Author/s:
Melia, HA;Dean, JW;Smale, LF;Illig, AJ;Chantler, CT

Title:
Count-rate, linearity, and performance of new backgammon detector technology

Date:
2019-05-01

Citation:
Melia, H. A., Dean, J. W., Smale, L. F., Illig, A. J. & Chantler, C. T. (2019). Count-rate, linearity, and performance of new backgammon detector technology. X Ray Spectrometry, 48 (3), pp.218-231. https://doi.org/10.1002/xrs.3024.

Count-rate, linearity and performance of new Backgammon Detector Technology

H A Melia

E-mail: h.melia@student.unimelb.edu.au

C T Chantler*

E-mail: chantler@unimelb.edu.au

L F Smale

E-mail: lucas.smale@gmail.com

A J Illig

E-mail: ajillig@gmail.com
School of Physics, The University of Melbourne, Melbourne Australia

Abstract. The meander wire Backgammon technology has high levels of flux and spatial linearity across a wide range of energies. One of the attractive features of these technologies is the stability of response and robustness under long X-ray exposure, the compactness and portability. A key problem historically has been the limited range of count-rate for processing to the optimum resolution. We report dramatic advances in this and other areas appropriate for high-accuracy experiments including tests of quantum electrodynamics, fundamental relativistic atomic physics, X-ray calibration and crystallography. We illustrate this technology applied to the K$\alpha_{1,2}$ spectra of titanium, chromium and copper. The quality of the spectra permit deeper insight into atomic and solid state science, and permits accurate measurement of energy and relativistic atomic physics processes, below 1μm accuracy or down to 1 part per million in energy.

1. Introduction

The invention and development of the multiwire gas proportional counters (MWPC) in 1968 [1, 2, 3] led to the widespread use of these types of detectors across numerous fields. Of note are the investigation and discovery of new fundamental particles [4, 5], which have led to several Nobel Prizes. MWPC have also been successfully implemented in astrophysics [6], X-ray spectroscopy [7] and protein crystallography [8].

Improvements on the original design of MWPCs have been achieved through better understanding of both theory and experiment. Theoretical modelling of electrostatic

effects inside the chamber [9], and induced charge on the wires [10] have led to a greater understanding of electronic processes, paving the way for improvements in the geometry and design of these detectors. A deeper understanding of the ionisation processes due to X-ray absorption inside the chamber from experiment has helped determine optimum operating conditions and improved resolution [11, 12, 13]. Furthermore the Backgammon cathode board geometry has led to an increase in spatial resolution in two dimensional position sensitive detectors [14].

The technology was developed further at NBS to a useful size of 38 mm [15, 16]. This backgammon technology has developed with improved resolution and linearity, as well as driving ideas in detector physics worldwide [17, 18, 19]. More recently the position resolution of MWPC have been shown to be comparable to charge coupled devices when used in similar experimental conditions [20].

Charged coupled devices (CCDs) can have significantly better spatial pixel resolution due to the binary pixel size of e.g. 20 μm; however, they are highly damage-sensitive [21, 22], highly non-linear, and only operating over quite modest dynamic ranges for flux. Also, there is a challenge for single-photon-counting or event-mode operation at normal fluxes, and poor real-time energy discrimination [23, 24]. After some time, the typical damage features require complex algorithms and beam-time for in situ calibration and mapping [23, 24] or replacement. Solid state detectors (germanium and lithium-drifted silicon detectors), now segmented, have much higher energy resolution, relatively robust and decent linearity of flux ranges but quite poor spatial resolution (pixel size often several mm). Conversely, beautiful new solid state detector technologies in these areas include the Maia detectors (CSIRO) [25], the Pilatus detectors (PSI) [26, 27] and the Eiger detectors (PSI) [28], with typical pixel sizes of 172 μm or 75 μm. These have been proven to have beam damage-resistance to a high level, with exceptional dynamic range or linearity in flux, and reasonable spatial resolution. Sometimes the cost towards several $100,000 is significant in comparison with a backgammon detector which can be fabricated in the laboratory at a small fraction of this cost. The choice of detector will always depend on the purpose and application, and the solid state detectors can achieve high spatial resolution and relatively poor linearity (CCDs) or low spatial resolution and extremely high linearity (e.g. Pilatus, Si(Li)).

Backgammon detectors have advantages of compactness, price and portability, together with good spatial resolution and excellent linearity. Perhaps more particularly, backgammon technology is ideal for soft X-ray spectroscopy and even toward in-vacuum technology, e.g. below 5 keV - 8 keV, where solid state detectors have low efficiency due to the windows, dead-layer, and gold contacts. The capacity to change the gas and gas pressure is a major advantage at these low energies where the absorption coefficient is increasing rapidly. However, one key challenge in earlier technology has been the flux limitation, particularly because of the charge or time-division and the arrival time of photons. We describe how this has now been improved dramatically by gating, data collection and software processing, so that these detectors are ideally suited to many applications including high-accuracy experimental tests of Quantum Electrodynamics,

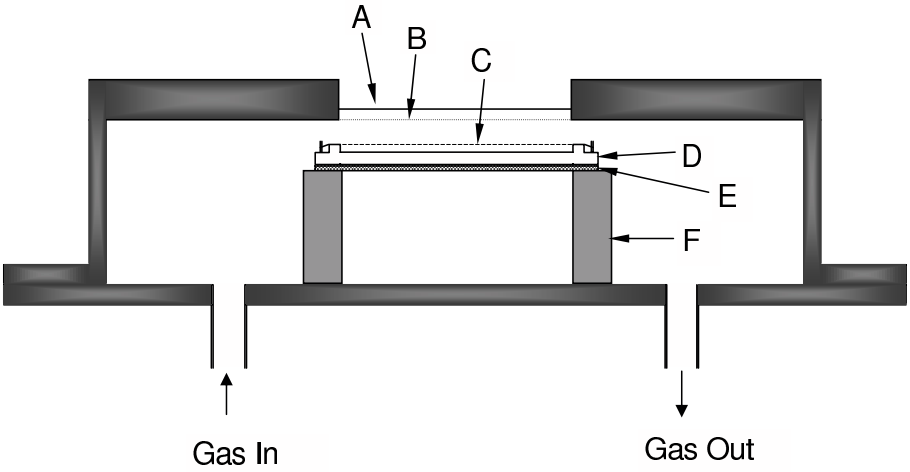

Figure 1. Cross section of the internal components of the UM Backgammon detector. A: the beryllium window. B: nickel mesh ground plane. C: platinum anode wire plane. D: Anode wire Macor frame. E: cathode board. F: Macor support structure.

relativistic atomic and solid state physics, and crystallography.

2. Experiment and key characteristics

The operation of the University of Melbourne (UM) Backgammon detector (Fig. 1) relies on three main components: The anode wire; the ionising gas that fills the detector; and the backgammon cathode board. As X-rays pass through the gas, atoms of the gas are ionised and an electron avalanche is created along with ionised atoms. The potential difference accelerates the positive gas ions towards the anode wire, with electrons accelerated towards the cathode board producing a current. The principle of resistive charge division is used to determine the position of the avalanche along the anode wire, while the avalanche position on the backgammon cathode board is determined by capacitative charge division on the segmented detector. A diagram of the cathode board and anode wire along side one another is shown in Fig 2. Fig. 3 shows a photograph of the anode wire and cathode board. The sawtooth shape of the cathode board gives the detector its name. The ionising gas in the detector for these experiments was P10 (90% argon and 10% methane) at a voltage of 2100 V and pressure of approximately 1060 Torr (slightly above atmospheric pressure). Investigations have been made at a range of pressures and voltages and also with Xenon-methane, which is preferable for high energy detection. For very low photon energy, nitrogen gas is useful for a high detector quantum efficiency.

Technical details of the UM Backgammon detector electronics and processing are in Appendix Appendix A. Appendix Appendix B provides details on cathode board and anode wire signal processing and calibration.

The X-ray Optics group at the University of Melbourne have improved the backgammon MWPC design over the last decades. The identification of systematics

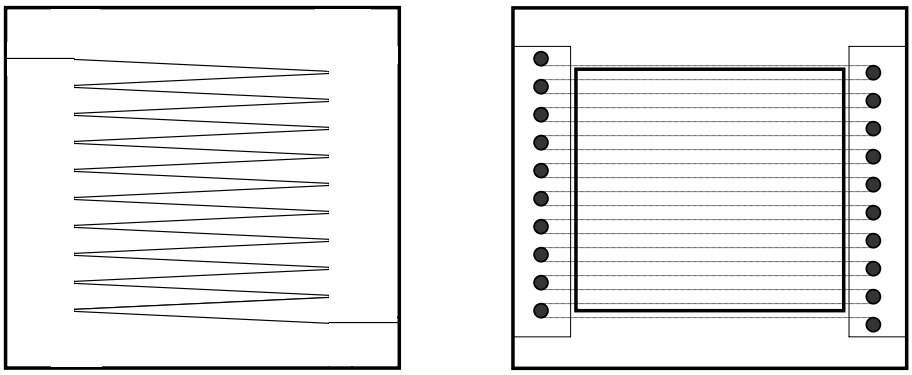

Figure 2. The left panel shows the segmented cathode board, separated by a 100 μm wide channel. The anode wire, shown on the right, is wrapped around gold-coated pins mounted to the Macor frame.

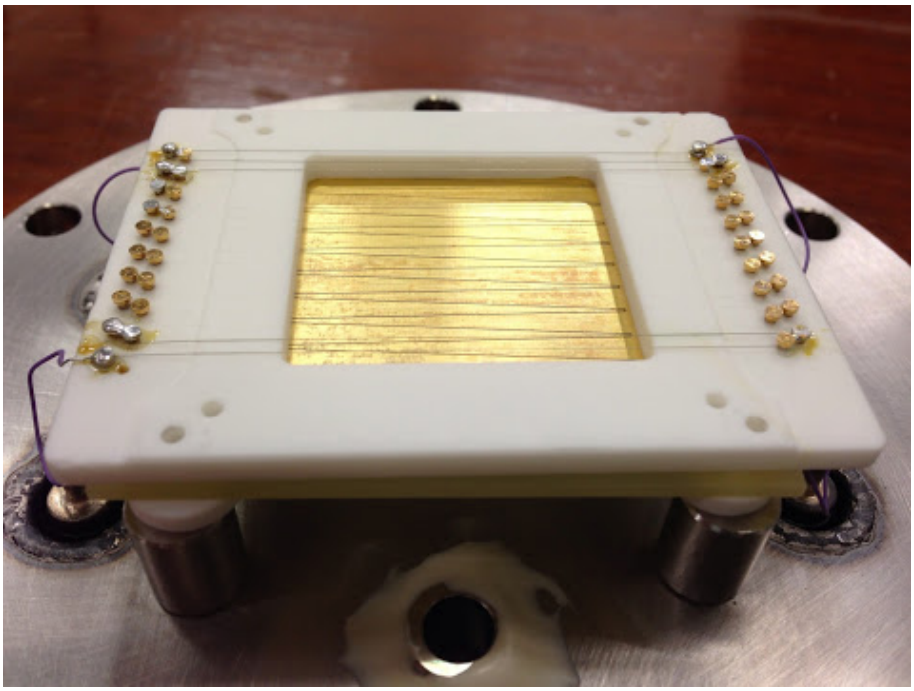

Figure 3. The cathode board and anode wire. The anode wire has been only partially strung so that the cathode board's backgammon shape can be seen. The gold coated pins suspending the wire are shown, as well as the four output wires.

thought to be inherent to these detectors has led to a reduction in image distortions and a dramatic improvement in resolution [20]. Improvements to the electronics of the backgammon detector have resulted in improved acquisition efficiency, diagnostic capability and correction time [29, 30]. Simulation of non-linear effects have led to a 20% increase in the linear active region and an increased photon detection efficiency of 326% [31]. In 2010 charge cloud modelling by Payne *et al.* was used to improve linearity [32]. Event-mode data collection is now normal. This paper highlights the application, advantages and utility of the most recent University of Melbourne (UM) Backgammon

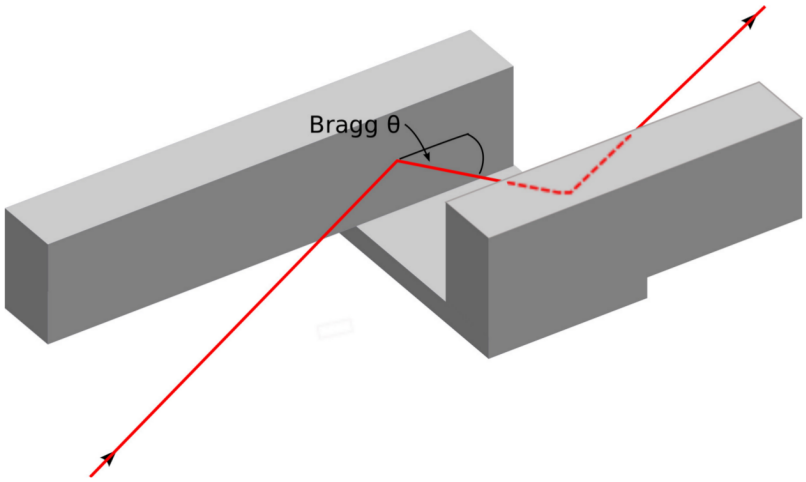

Figure 4. The Si(111) double bounce monochromator. The Bragg angle and the X-ray beam path are shown.

detector. The UM Backgammon detector has been tested in terms of flux linearity, spatial linearity and spatial resolution.

2.1. Flux linearity

Characteristic X-ray radiation was generated by a MAC Science SRA M18XH1 water cooled rotating anode source. A 10 mA current was passed through a tungsten filament producing a stream of electrons incident on a Cu anode. X-rays exit the rotating anode through a 1.0 mm slit and into a collimator. The collimator consisted of a 244 ± 3mm length lead pipe with 1.0 mm slit at the end. Once collimated, the beam was diffracted using a monolithic Si(111) channel-cut crystal (Fig. 4). After being dispersed by the monochromator, the spectrum was attenuated with aluminium foils and projected onto the beryllium window of the UM Backgammon detector (Fig. 5). Lead panels shielded the detector face from scattered X-rays. For each attenuating thickness, the number of X-ray events detected over 10 seconds was recorded and the count rate determined. Thirteen thicknesses were examined ranging from 16 to 192 foils with 12 μm per foil.

The count rate was modelled assuming that the detector count rate responds linearly to X-ray intensity and that the X-ray beam was composed of two components: the Cu Kα spectrum and a first order harmonic component. The count rate in Hertz, I, is given as a function of the attenuation thickness, measured as the number of 12 μm foils, n: $I = I_0(1-h_f)e^{-\mu_1 tn} + I_0 h_f e^{-\mu_2 tn}$. I_0 is the incident count rate, the X-ray intensity times the detector efficiency; t is the thickness of the Al foils used; h_f is the fraction of the incident count rate due to the harmonic (higher energy) component of the beam. μ_1 and μ_2 are the linear attenuation coefficients of Al for the energy of Cu Kα, 8.04 keV and its first harmonic respectively for 16.08 keV. Values for $[\frac{\mu}{\rho}]_{1,2,3}$ are

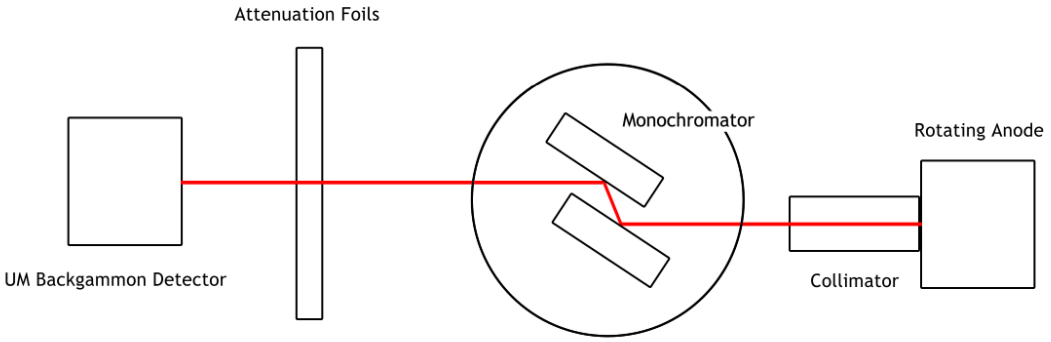

Figure 5. Diagram of the rotating anode experimental setup. The rotating anode, collimator, monochromator, aluminium attenuation foil and UM Backgammon detector are represented. The X-ray beam is collimated with 1 mm slits at each end of the collimator.

48.411, 6.23, 1.99 cm^2/g [33]. Hence values for $\mu_1 = [\frac{\mu}{\rho}]_1\rho$, μ_2 and μ_3 for aluminium foils are $\mu_{1,2,3}$ are 130.43, 16.79 and 5.36 cm^{-1}. The experimental data agree perfectly with the coefficients for μ_1 for the initial slope and with μ_2 for the higher harmonic, within 3-6%, confirming that the higher harmonic is definitively not from the 333 reflection but is from the 222 reflection. It is in fact impossible to have the expected normally dominant third order radiation (second harmonic) because the accelerating voltage is only 20 keV. We observe the direct attenuation of the beam with foil thickness with the attenuation coefficient exactly that of the forbidden second order Si 222 reflection. This reflection is forbidden i.e. suppressed - it is non-zero due to the silicon bonding, as discussed in the International Tables for Crystallography Volume C [34]. The intensity of the first harmonic (222) compared to the fundamental (111) can be obtained through the structure factors of Si 111 and 222: $(F_{222}/F_{111})^2 = \left(\frac{1.85\pm0.85}{59.87\pm0.46}\right)^2 \approx (0.1 \rightarrow 0.2)\%$ [35].

Fitting the model to the data gives $\chi_r^2 = 1.3$ and plausible values for all parameters (Fig. 6, Table 1). A good χ_r^2 indicates that the count rate is linear from 7 Hz up to at least 17 kHz and that the X-rays incident on the detector are composed of a Cu Kα component and a higher energy component, from second order Bragg diffraction. We also obtain the dark current to be 4±1 Hz.

The fitted effective harmonic percentage represents the product of the overall detector efficiency and optic losses compared with that of the fundamental (8.04 keV) energy, multiplied by the actual harmonic percentage. This has been discussed elsewhere [36]; note that the air absorption is negligible so that the differential efficiency is dominated by the source, detector and window components. The amplitude of the spectral intensity will vary from first order to second order. For a typical fixed anode source the peak amplitude is stronger for the characteristic Kα radiation than for the

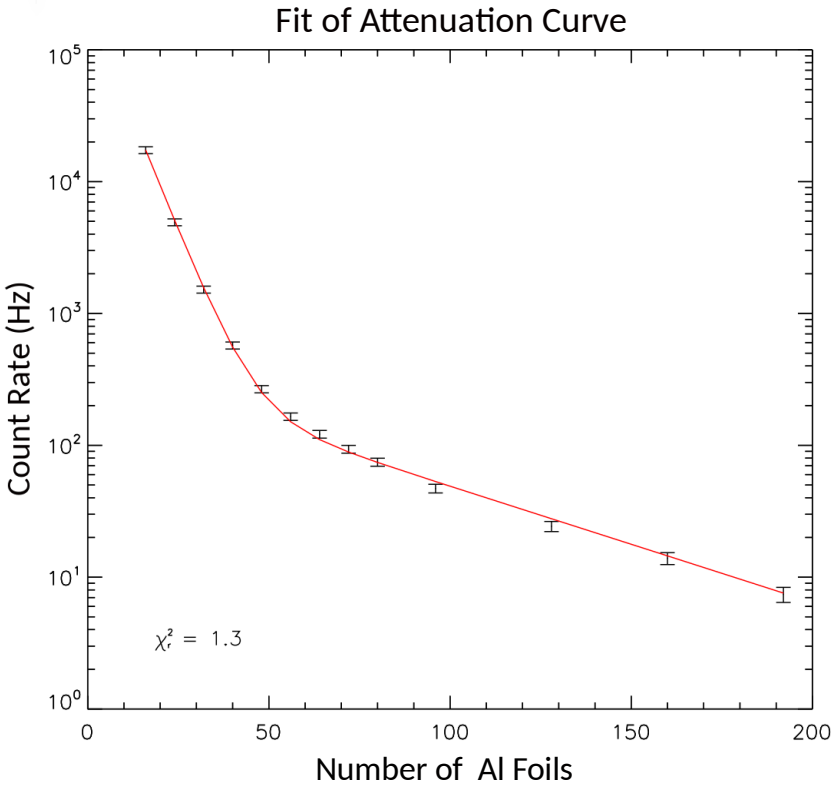

Figure 6. Flux linearity across 4 decades. This log-linear plot of attenuation shows a clear signature of two energy components attenuated by the foil thicknesses, with each foil thickness $\approx 12\mu$m. The first straight section reflects the higher attenuation coefficient component (Cu Kα), while the second reflects the lower attenuation coefficient component - the higher energy first harmonic component.

Parameter	Fitted value	Standard deviation σ, s.d.
I_0	213 kHz	21 kHz
t	12.07 μm	0.29 μm
h_f	0.175%	0.011%

Table 1. Fitted parameters with uncertainties for Eqn C.1 for count rate verses thickness. t represents the thickness per foil, consistent with previous measurements.

bremsstrahlung first harmonic; for a synchrotron source the peak source ratio might be within a factor of two; for a typical laboratory X-ray source such as ours, the source ratio is strongly affected by the takeoff angle, self-absorption and the optical bandpass. The detector efficiency is also critically dependent upon the dead region common in all (backgammon) detectors. We have observed the 222 reflection in similar laboratory experiments with alternate detectors, so that the fitted *effective percentage* of 0.175% is quite reasonable.

2.2. Spatial linearity

Non-linearities in the spatial response in the energy dispersive direction in an X-ray detector lead to systematic errors in the energy calibration of the spectrometer system and measurement. The backgammon detector type has a great advantage in this respect over large pixel-based detectors because the spatial signal is analogue so that the linearity does not have a binary minimum spatial extent. A spatial calibration map for the detector was developed to map the raw output of the detector to a physical length scale, in the cathode board axis (Appendix Appendix C).

The *maximum fractional non-linearity* is defined as the maximum residual between the detector output, x, and physical length, L, at which the event took place, divided by the total length of the active region of the detector. The maximum fractional non-linearity of our detector was found to be 0.016 mm /22 mm = 0.073%. This is a significant improvement on the previous best backgammon designs which report a maximum fractional non-linearity of 0.2% [29]. For comparison the detector used in the current best X-ray emission spectra experiment has a pixel size of 172 μm giving an average spatial non-linearity of 86 μm, much larger than our maximum spatial non-linearity of 16 μm. The maximum fraction non-linearity is the maximum extreme outlier for a single channel and is not representative of a typical uncertainty in the detector cathode position response. This overestimate of the extreme non-linearity can be dominated by statistical outliers, generally towards the edge of the detector.

Non-linearity can also be quantified by looking at the *fractional linearity uncertainty* in the fitted parameters over the linear relation, the gradient and the offset. This measure gives an indication that, subject to noise, a broad feature can be resolved to high accuracy.

In our case the effective non-linearity is perhaps best defined by the *regional non-linearity*, defined as the average deviation of the detected centroid from the linear fit. This measure represents the typical error of a single channel position determination, rather than the most extreme point-defect or statistical error. From Appendix Appendix C, this is of order 1 μm across the full range of the detector, corresponding to an energy accuracy of order 2 ppm or less for Cu Kα. The overall accuracy of an experiment does not only depend on the detector used. The final accuracy, in parts per million, should account for all types of uncertainties and the ppm quoted here is only one such systematic. However, the detector non-linearity will always contribute to this total uncertainty and is therefore an important specific of the UM backgammon detector.

3. Experiment: Relativistic atomic physics of characteristic radiation

The backgammon type MWPCs developed at the University of Melbourne have been successfully used in experiments including tests of quantum electrodynamics (QED) and high accuracy measurement of X-ray spectra [7, 37, 38]. We present three new studies to illustrate the characteristics and utility.

The UM Backgammon detector recorded the X-ray spectra of Chromium and Titanium from a Johann-type curved crystal X-ray spectrometer, operating at a near vacuum pressure, less than 10^{-7} Torr. The characteristic X-ray radiation was generated using a fluorescence source, being a 20 keV electron gun and a metal target (Fig. 7). The electrons incident on the metal target create the corresponding Kα radiation.

The radiation is diffracted using a Ge(220) curved crystal monochromator and projected onto the detector face at the end of the detector arm. The electron gun beam was normal to both the metal target-to-crystal and crystal-to-detector X-ray beams. The detector was placed 1.5 m from the crystal monochromator, each positioned on the Rowland circle to ensure the focusing and maximum intensity of X-ray photons (Fig. 8). Fig. 8 illustrates the target element, the 2θ angle of the detector arm, and the adjustable wedge which can alter bandpass, instrumental broadening (vignetting) and other spectral systematics.

The detector arm angle was measured by 2 gravity-referenced clinometers, with voltage as the raw output. These were placed at the base and top of the detector arm. Before the experiment each had been calibrated against a Heidenhain ROD 800 interferometric encoder using a Huber 410 goniometer. A Huber SMC 9000 motor controller controlled the angular motion. For each element, 3 runs were performed, with runtimes of roughly 20 minutes giving the number of counts at the peak of the spectra in the order of 10^4. For each run, the detector arm was rotated slightly so the spectra would be incident on different positions along the detector face. This defined clinometer calibration and the 2θ angle. The detector outputs two-dimensional histograms showing the events measured across the detector face (Appendix Appendix A).

The 2D histograms show the distribution of the photon-gas interaction on the detector face. Values in each x-channel were summed to yield one-dimensional spectra with counts as function of x-channel. The monochromator, relates x to energy. Each spectra was summed after calibration using a calibration map from a slit-illuminated source (Appendix Appendix C).

4. Profile Analysis and Quality of Spectra

The best measurement available of the chromium Kα spectrum [39], was characterised by fitting the sum of six Lorentzian functions to the data after a deconvolution.

Two characterisations of the titanium Kα spectrum are presented [37]. Each has been found by fitting the sum of 6 Voigt functions, with a common Gaussian broadening term, to data previously published [40, 41]. These parameterisations are considered the best thus far.

The quality of the fluorescent source and UM Backgammon detector were tested by measuring chromium and titanium data collected. Most large-pixel detectors cannot be mounted on the detector arm in this vertical orientation of the spectrometer because of their weight and bulk. A Levenberg-Marquardt fitting procedure fitted Voigt profile characterisations following [39, 37]. The energy scale was calibrated by the energy

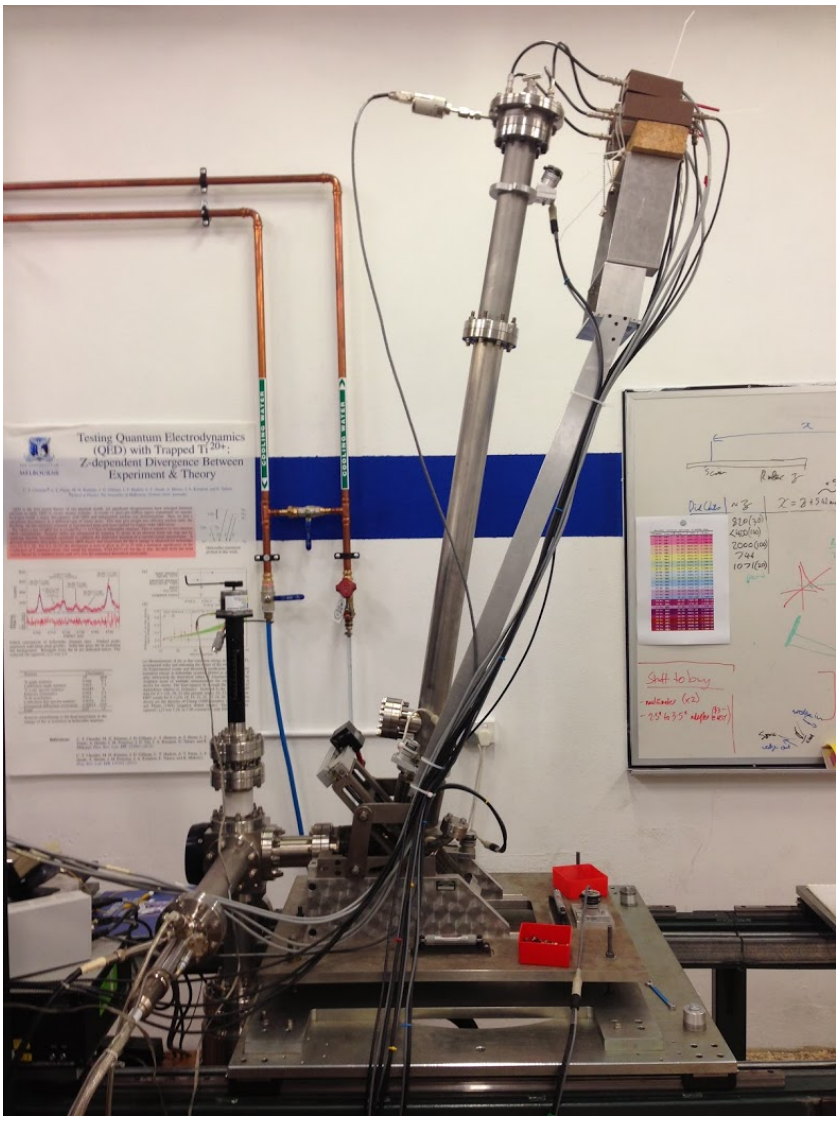

Figure 7. Fluorescent source experimental set-up, used to obtain spectra of Cr and Ti. The UM Backgammon detector can be seen at the end of the detector arm, as well as the electron gun normal to the target-crystal beam running across the page.

difference between Kα_{11} and Kα_{21}. Common Gaussian and Lorentzian widths capture instrumental broadening.

Figs 9 and 10 show our data parameterised by these state-of-the-art measurement standards. Fitting the Cr spectrum yielded $\chi^2_r = 2.20$. Fitting the Ti spectrum yielded $\chi^2_r = 1.67$. Both indicate excellent resolution, profile consistency and linearity. Both spectra show two well separated peaks, no signs of non-linearities, low noise and residuals typical of X-ray spectra. Any instrumental broadening has been modelled using Voigts rather than Lorentzians. Even with our modest broadening, our Cr Kα spectrum compares quite well with Fig. 1 a) from [39]. A low χ^2_r indicates that our data is consistent with spectra obtained using the best solid state detectors available. Both indicate some correlated noise in the residual, which is also characteristic of the earlier

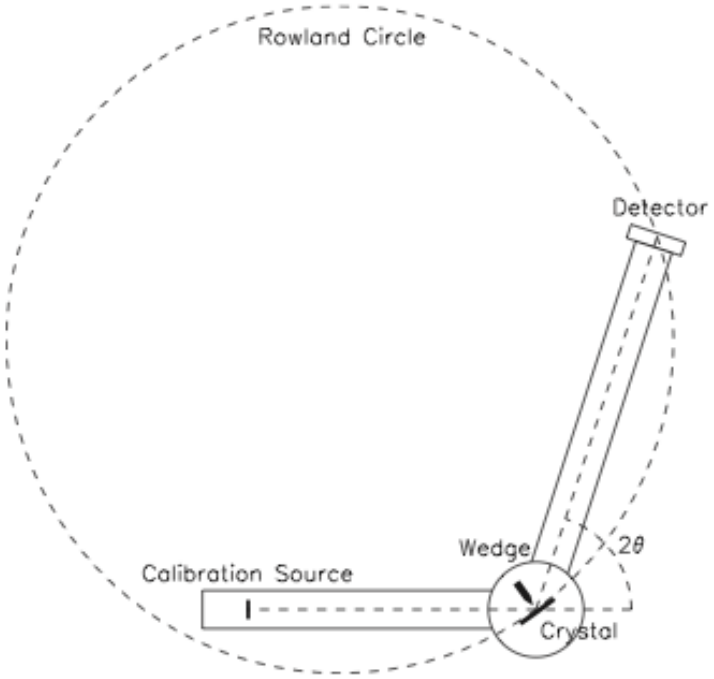

Figure 8. Schematic diagram of the fluorescent source experimental setup, used to obtain the spectra of Cr and Ti.

world best characterisations. This high level probe of X-ray structure, relativistic atomic physics, and of calibration standards and methodology is important for standard X-ray sources and advanced experiments. This demonstrates clearly the capability of the UM Backgammon detector to measure characteristic and general X-ray spectra comparable to the state of the art for any detection system.

The resolution of a detector, when used in X-ray spectroscopy, allows the determination of individual components in the spectra. The total broadening present in our data can be quantified by looking at the common broadening of the fits. This total broadening is made up two parts: the instrument function psf (point spread function) inherent to the spectrometer itself, and the broadening (psf) due to the detector resolution. The instrumental broadening function or point spread function (PSF) of the spectrometer was estimated using dynamic diffraction modelling *Mosplate* [42, 43, 44]. The detector broadening (psf) was a consistent residual after the removal of the instrumental broadening function in quadrature, of 240 μm with an estimated uncertainty of $\pm$ 20 μm. This is a significant improvement on the resolution of 330 μm $\pm$ 30 μm of earlier designs [29].

5. Experiment: Copper Kα and rotating anode spectra

The UM Backgammon detector also investigated the X-ray spectrum of copper metal in a qualitatively different experimental setup using the University of Melbourne rotating

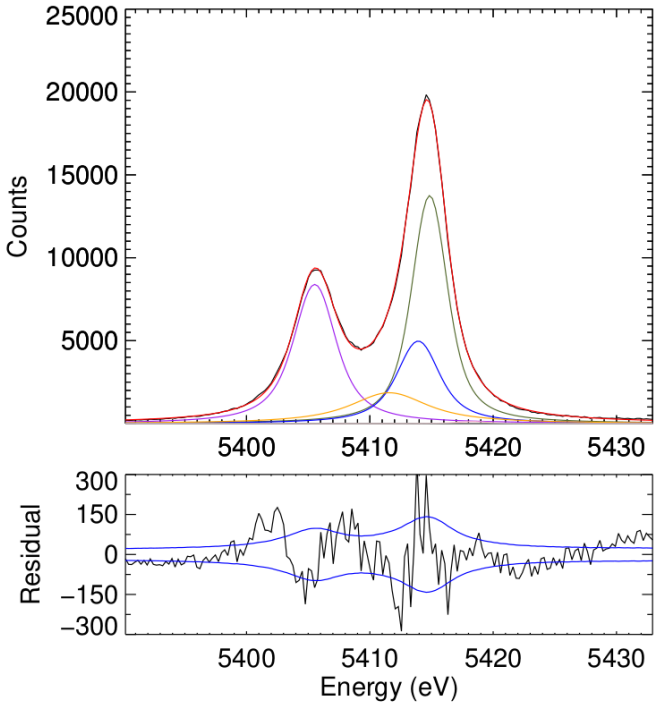

Figure 9. High-resolution spectral profile of Cr Kα obtained with the UM Backgammon detector, with excellent fit to the current best characterisation of Cr Kα ($\chi^2_r = 2.20$); [39, 37]. The profile, above, indicates the component peaks from the characterisation. The residuals in black, below, are compared with the 1-standard error envelope in blue. Some correlated residual noise is observable, as found in the data sets of the reference characterisations with different source and detector optics.

anode. Characteristic X-ray radiation was generated by a MAC Science SRA M18XH1 water cooled rotating anode source. The Si(111) crystal has a lattice, $d = 3.1356$ Å. This gives a Bragg angle for Kα_1 of 14.219° and 14.258° for Kα_2. These correspond to energies of 8047.78 eV and 8027.83 eV, respectively. The angle between the X-ray and the double bounce Si(111) monochromator normal (Fig. 4) was set between these angles. After being dispersed by the monochromator, the spectrum was attenuated with aluminium and projected onto the beryllium window of the UM Backgammon detector. Lead panels shielded the detector from scattered X-rays (Fig. 5).

The detector was set to a voltage of 2100 V, using P10 (90% argon and 10% methane) as the ionising gas. Multiple profiles of the Cu Kα spectrum were taken with exposure times of 7200 s. The rotating anode voltage was set to 20 kV, where the Kα spectrum has been shown to be stable [45]. A highly attenuated background exposure was also taken, only allowing residual high energy X-rays to reach the detector face, to separate fundamental and higher order scattered radiation (Appendix Appendix D). Table 2 summarises the measured profiles.

The Cu spectrum was obtained from the raw data in the same manner as the Cr and Ti spectra. Fig. 11 shows the well resolved Cu spectrum. The amount of

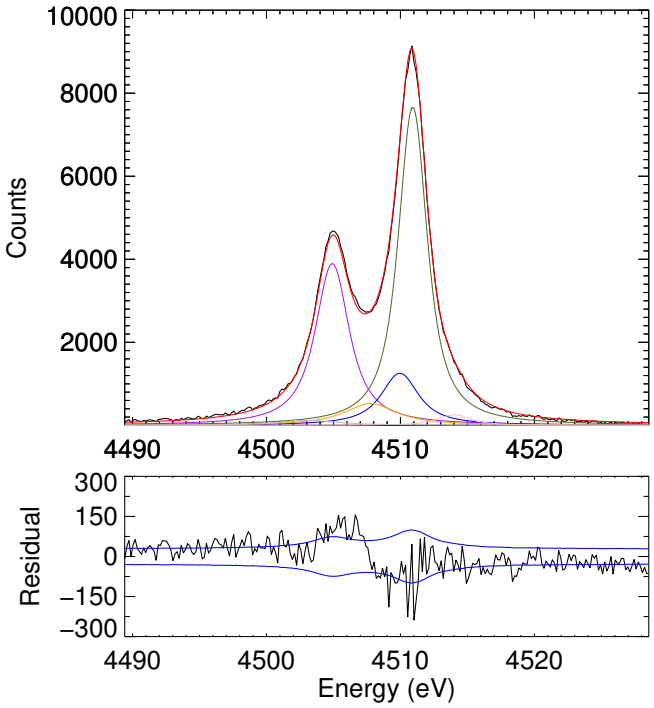

Figure 10. High-resolution spectral profile of Titanium Kα obtained with the UM Backgammon detector, with excellent fit to the current best characterisation ($\chi^2_r = 1.67$); [37].

	no of Foils	Exposure time Seconds	Current mA	Total Counts	Frequency Hz
File 1	32	7200	14	6553428	910.2
File 2	24	7200	10	8339156	1158.2
File 3	24	7200	10	8343119	1158.8
Background	104	1200	200	1506841	1255.7

Table 2. Experimental details of the Cu Kα measurements. The frequency column shows the rate at which X-ray events were counted.

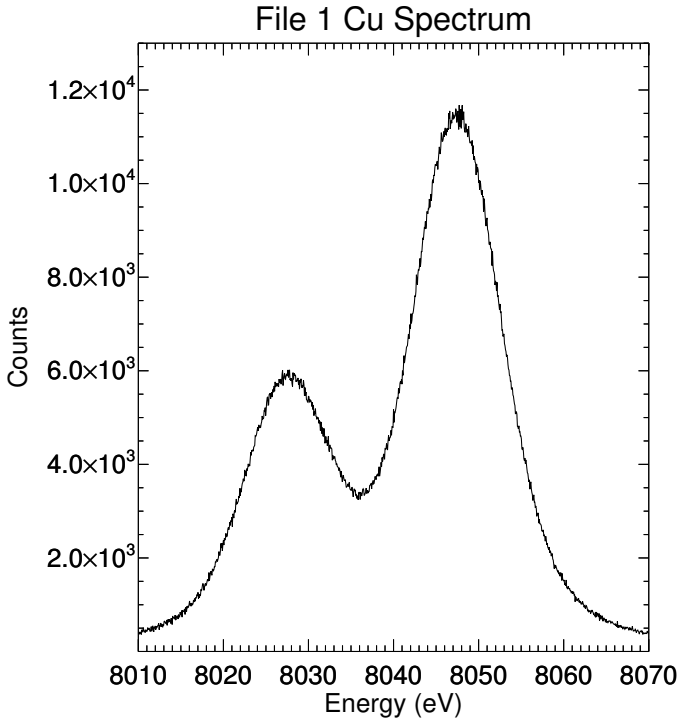

Figure 11. The good resolution spectral profile of the File 1 Cu Kα data, obtained from the rotating anode and UM Backgammon detector. The Kα_1 and Kα_2 peaks are well separated.

instrumental broadening in X-ray spectra is different for each experiment, depending upon the experimental geometry, spectrometer instrument function and divergence. To compare our data to literature spectra, the broadening is removed using a deconvolution [39]. This assumes that the broadening is uniform across the spectrum. For the Cu file 1 data, shown in Fig. 12, the amount of Gaussian and Lorentzian broadening removed was 9.243 and 2.852 eV respectively. The quality of the spectra again demonstrates the UM Backgammon detector capability.

The deconvolved Cu spectrum (Fig. 12) compares well with Cu X-ray spectra from literature [46]; their Fig 4 displays the deconvolved Cu Kα spectra. More recently the Cu Kα has been measured using a Pilatus 100K solid state detector [47]. Our results (Fig. 12) also match well with those in Fig. 19 of their publication. This detector technology is able to measure X-ray spectra consistent with the current best technologies and long lasting literature standards. In particular, the analogue measurement enables a continuous spectral representation with an accuracy to below 1 part per million in

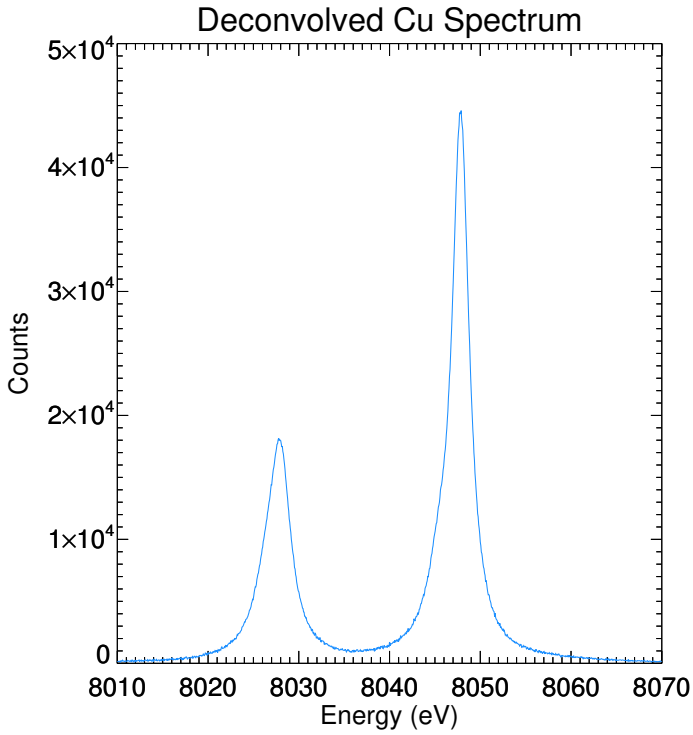

Figure 12. The deconvolved spectrum compares extremely well to published literature [46, 47].

energy (0.0001%).

6. Discussion

Quantum electrodynamics is the current best description of the interaction between electromagnetic radiation and electric charge. Discrepancies between experimentally measured energies of the lamb shift and those predicted by theory are key in many tests of QED. One probe is to look at hydrogen-like and helium-like medium Z ions, as here the scaling of corrections allow feasible precision, and low nuclear effects. These tests require detectors capable of highly accurate energy determination across a range of fluxes. The UM Backgammon high degree of spatial linearity makes it capable of measuring energies to a few parts per million, as well as being highly linear in terms of count rate. Coupled with a satisfactory resolution the UM Backgammon detector is well suited to such QED tests as well as high accuracy X-ray spectroscopy experiments.

A maximum fractional non-linearity of 0.073% amounts to a significant

	Z	Kα_{11} Energy (eV)	χ^2_r	Gaussian width (eV)	Lorentzian width (eV)
Titanium	22	4510.926 ± 0.014	1.54	1.018 ± 0.025	0.786 ± 0.025
Chromium	24	5414.874 ± 0.002	2.20	2.049 ± 0.015	0.782 ± 0.021
Copper	29	8047.837 ± 0.002	2.08	9.243 ± 0.018	2.852 ± 0.020

Table 3. Widths and energies with standard deviation uncertainties and χ^2_r of fits using the current literature standards with instrumental broadening indicated from the source, optic, spectrometer and detector configuration. Results for Cu are for File 1 data taken with the rotating anode source. Low χ^2_r across different experimental geometries and energies highlights the detectors utility.

improvement on the best previous designs, that demonstrate a maximum fractional non-linearity of 0.2% [16, 29]. The regional non-linearity implies accuracies to 1 μm and below, and clearly permits measurement accuracies to sub-μm and of order 1 ppm. The fractional non-linearity of our detector, regardless of which measure you consider, is significantly smaller than that achievable by the best solid state available. A pixel size of 172 and 75 μm, for the Pilatus and Eigar detectors respectively, means that non-linearities of 86 μm and 37.5 μm are quite significant for high-accuracy measurement.

A sophisticated data acquisition system for our detector enables single photon counting and efficiencies over a range of flux, 1Hz-50kHz (see Appendix Appendix A). The UM Backgammon detector has been shown to be linear in intensity up to at least 17 kHz. This is especially significant when comparing to CCD non-linearities at high count rates or over intensity ranges above two decadal ranges.

The Cr and Ti data, taken with the fluorescence source, have been fitted following [39, 37] with excellent χ^2_r indicating that data obtained with the UM Backgammon detector, is consistent with that published in the literature. Table 3 indicates that the broadening present is not significant for the Ti and Cr spectra.

The Cu spectrum, measured using the rotating anode laboratory source, was also fitted using one of the current best parameterisations available [39]. The Cu spectra (Fig. 11) contains a higher instrumental broadening from source and monochromator compared to those taken with the fluorescence source (Figs 9, 10), and fits well in this alternate experimental setup. A low χ^2_r demonstrates the robustness of the detector over a range of energies and experimental geometries.

7. Conclusion

Experiments striving to probe phenomena at increasing levels of sensitivity rely on advanced detectors. The collected data for the Kα splitting of copper, chromium, and titanium, and the capacity to make critical tests of quantum electrodynamics, demonstrate that the University of Melbourne Backgammon detector is capable of recording highly accurate X-ray spectra over a wide range of energies. The collected data is comparable, and superior in several respects, to those taken with charged coupled devices that have sometimes been preferable in certain fields of experimental physics.

The regional non-linearity of 1 μm allows the detection of photons to be readily determined down to 1-2 part per million in energy, an improvement on similarly designed MWPC detector devices. Furthermore, the ability to alter the gas that fills the detector and the ionisation mechanism ensures that a wide range of photon energies can be resolved at similar resolution. Also significant is the quality fitting of data using the best available parameterisations. Low χ_r^2 show that the quality compared with what has previously been published despite different experimental conditions, setups and detector geometry. After the removal of common broadening, the spectra recorded in the described experiments match well those previously published. The detector allows previous experiments to be used as calibrations for future experiments, with the raw calibration of incident photon position on the detector face and improvements to the data analysis and processing. The popularity of MWPCs in X-ray spectrometry and other areas of measurement science remains very strong.

8. Acknowledgements

We acknowledge A. T. Payne for his part in the development of the Backgammon detector technology and of the data acquisition. We acknowledge the group of X-ray Optical and Synchrotron Science at the School of Physics.

References

[1] G. Charpak, R. Bouclier, T. Bressani, J. Favier, and Č. Zupančič, "The use of multiwire proportional counters to select and localize charged particles," *Nuclear Instruments and Methods*, vol. 62, no. 3, pp. 262–268, 1968.

[2] G. Charpak, D. Rahm, and H. Steiner, "Some Developments in the Operation of Multiwire Proportional Chambers," *Nuclear Instruments and Methods*, vol. 80, pp. 13–34, 1970.

[3] G. Charpak and F. Sauli, "High-Accuracy, Two-Dimensional Read-Out in Multiwire Proportional Chambers," *Nuclear Instruments and Methods*, vol. 113, pp. 381–385, 1973.

[4] B. Richter, "From the psi to charm: The experiments of 1975 and 1976," *Rev. Mod. Phys.*, vol. 49, no. 2, pp. 251–266, 1977.

[5] C. Rubbia, "Experimental observation of the intermediate vector bosons W+, W-, and Z0*," *Rev. Mod. Phys.*, vol. 57, no. 3, pp. 699–722, 1985.

[6] L. Horton, J. Ulrichs, and M. Winn, "The use of multiwire proportional counters in a cosmic ray air shower experiment," *Nuclear Instruments and Methods in Physics Research A*, vol. 325, no. 1993, pp. 326–334, 1992.

[7] C. T. Chantler, D. Paterson, L. T. Hudson, F. G. Serpa, J. D. Gillaspy, and E. Taka, "Absolute measurement of the resonance lines in heliumlike vanadium on an electron-beam ion trap," *Physical Review A*, vol. 62, pp. 1–13, 2000.

[8] F. Ortuno-Prados, A. Bazzano, A. Berry, C. Budtz-Jorgensen, C. Hall, W. Helsby, R. Lewis, B. Parker, and P. Ubertini, "A high-pressure MWPC detector for crystallography," *Nuclear Instruments and Methods in Physics Research A*, vol. 420, pp. 446–452, 1999.

[9] G. A. Erskine, "Electrostatic problems in multiwire proportional chambers," *Nuclear Instruments and Methods*, vol. 105, pp. 565–572, 1972.

[10] G. A. Erskine, "Charges and current induced by moving ions in multiwire chambers," *Nuclear Instruments and Methods*, vol. 198, pp. 325–336, 1982.

[11] G. C. Smith, J. Fischer, and V. Radeka, "Resolution for X-rays in gas proportional chambers;," *IEEE Transactions on Nuclear Science*, vol. NS-31, no. 1, pp. 111–115, 1984.

[12] J. Fischer, V. Radeka, and G. C. Smith, "X-ray Position Detection in the region of 6 μm RMS with Wire proportional Chambers*," *Nuclear Instruments and Methods in Physics Research A*, vol. 252, pp. 239–245, 1986.

[13] J. Fischer, V. Radeka, and G. C. Smith, "Position Detection of 17-25 keV X-Rays In Krypton and Xenon With a Resolution of 18-50um (FWHM)*," *IEEE Transactions on Nuclear Science*, vol. 33, no. 1, pp. 257–260, 1986.

[14] R. Allemand and G. Thomas, "Nouveau detecteur de localisation," *Nuclear Instruments and Methods*, vol. 137, no. 1, pp. 141–149, 1976.

[15] B. P. Duval, J. Barth, R. D. Deslattes, A. Henins, and G. G. Luther, "Position-sensative X-ray detector," *Nuclear Instruments and Methods in Physics Research*, vol. 222, pp. 274–278, 1984.

[16] G. G. Luther, P. L. Cowan, A. Henins, and S. Brennan, "New two dimensional position sensitive proportional detecors using charge division," *Nuclear Instruments and Methods in Physics Research A*, vol. 246, no. 1, pp. 537–540, 1986.

[17] T. Mizogawa, M. Sato, and Y. Awaya, "Application of the ?mbwc? two-dimensional position readout technique to a multiwire proportional counter," *Nuclear Instruments and Methods in Physics Research Section A: Accelerators, Spectrometers, Detectors and Associated Equipment*, vol. 366, no. 1, pp. 129 – 136, 1995.

[18] G. Veshapidze, T. Nishide, H. Shiromaru, N. Kobayashi, and T. Mizogawa, "A time- and position-sensitive detector using a resistive film anode combined with a modified backgammon with weighted capacitors readout pad," *Japanese Journal of Applied Physics*, vol. 41, no. 2R, p. 871, 2002.

[19] T. Mizogawa, H. Shiromaru, M. Sato, and Y. Ito, "A two-dimensional position-sensitive ion detector based on modified backgammon method with weighted-coupling capacitors," *International Journal of Mass Spectrometry*, vol. 215, no. 1, pp. 141 – 149, 2002. Detectors and the Measurement of Mass Spectra.

[20] M. N. Kinnane, J. A. Kimpton, M. D. D. Jonge, K. Makonyi, and C. T. Chantler, "The correction of systematic image deformations inherent to two-dimensional proportional counters," *Measurement Science and Technology*, vol. 16, pp. 2280–2286, 2005.

[21] J. Janesick, T. Elliott, and F. Pool, "Radiation damage in scientific charge-coupled devices," *IEEE Transactions on Nuclear Science*, vol. 36, no. 1, pp. 572–578, 1989.

[22] N. Bassler, "Radiation damage in charge-coupled devices," *Radiation and Environmental Biophysics*, vol. 49, no. 3, pp. 373–378, 2010.

[23] L. T. Hudson, J. D. Gillaspy, J. M. Pomeroy, C. I. Szabo, J. N. Tan, B. Radics, E. Takacs, C. T. Chantler, J. A. Kimpton, M. N. Kinnane, and L. F. Smale, "Detection of faint X-ray features using wavelength, energy and spatial discrimination techniques," *Nuclear Instruments and Methods in Physics Research A*, vol. 580, pp. 33–36, 2007.

[24] L. F. Smale, C. T. Chantler, and L. T. Hudson, "The effects of cosmic ray filtering on low intensity X-ray CCD data," *Nuclear Instruments and Methods in Physics Research A*, vol. 619, pp. 150–153, 2010.

[25] D. P. Siddons, R. Kirkham, C. G. Ryan, G. De Geronimo, A. Dragone, A. J. Kuczewski, Z. Y. Li, G. A. Carini, D. Pinelli, R. Beuttenmuller, D. Elliott, M. Pfeffer, T. A. Tyson, G. F. Moorhead, and P. A. Dunn, "Maia X-ray microprobe detector array system," *Journal of Physics: Conference Series*, vol. 499, no. 1, 2014.

[26] C. Broennimann, E. F. Eikenberry, B. Henrich, R. Horisberger, G. Huelsen, E. Pohl, B. Schmitt, C. Schulze-Briese, M. Suzuki, T. Tomizaki, H. Toyokawa, and A. Wagner, "The PILATUS 1M detector," *Journal of Synchrotron Radiation*, vol. 13, no. 2, pp. 120–130, 2006.

[27] B. A. Sobott, C. Broennimann, B. Schmitt, P. Trueb, M. Schneebeli, V. Lee, D. J. Peake, S. Elbracht-Leong, A. Schubert, N. Kirby, M. J. Boland, C. T. Chantler, Z. Barnea, and R. P. Rassool, "Success and failure of dead-time models as applied to hybrid pixewl detectors in

high-flux applications," *Journal of Synchrotron Radiation*, vol. 20, pp. 347–354, 2013.

[28] R. Dinapoli, A. Bergamaschi, B. Henrich, R. Horisberger, I. Johnson, A. Mozzanica, E. Schmid, B. Schmitt, A. Schreiber, X. Shi, and G. Theidel, "EIGER: Next generation single photon counting detector for X-ray applications," *Nuclear Instruments and Methods in Physics Research, Section A: Accelerators, Spectrometers, Detectors and Associated Equipment*, vol. 650, no. 1, pp. 79–83, 2011.

[29] J. A. Kimpton, M. N. Kinnane, and C. T. Chantler, "Development of backgammon-type multiwire proportional counters for the detection of x rays," *Review of Scientific Instruments*, vol. 77, no. 8, pp. 1–7, 2006.

[30] J. A. Kimpton, M. N. Kinnane, L. F. Smale, C. T. Chantler, L. T. Hudson, and A. Henins, "Data acquisition system development for the detection of X-ray photons in multi-wire gas proportional counters," *Nuclear Instruments and Methods in Physics Research A*, vol. 580, pp. 246–249, 2007.

[31] A. T. Payne, J. A. Kimpton, M. N. Kinnane, and C. T. Chantler, "Simulation and minimization of nonlinear effects in backgammon-type multi-wire gas proportional counters," *Measurement Science and Technology*, vol. 20, 2009.

[32] A. Payne, J. A. Kimpton, L. F. Smale, and C. T. Chantler, "Optimisation of the spatial linearity in backgammon-type multi-wire gas proportional counters The relevance of charge cloud distribution," *Nuclear Instruments and Methods in Physics Research A*, vol. 619, no. 1-3, pp. 190–197, 2010.

[33] C. T. Chantler, "Theoretical form-factor, attenuation and scattering tabulation for z=1-92 from e=1-10 ev to e=0.4-1.0 mev," *Journal of Physical and Chemical Reference Data*, vol. 24, pp. 71–591, Jan 1995.

[34] U. W. Arndt, R. D. Deslattes, E. G. J. Kessler, P. Indelicato, E. Lindroth, D. C. Creagh, and J. H. Hubbell in *International Tables for Crystallography, Vol. C* (A. J. C. Wilson and E. Prince, eds.), ch. 4.2, X-rays, pp. 191 – 258, Dordrecht: Kluwer Academic Publishers, 1999.

[35] Y. Ando, A. Ichimiya, and R. Uyeda, "A determination of the absolute values and signs of the 111 and 222 structure factors of silicon," *Acta Crystallographica Section A*, vol. 30, no. 4, pp. 600–601, 1974.

[36] J. L. Glover and C. T. Chantler, "A method to determine the absolute harmonic content of an x-ray beam using attenuation measurements," *X-Ray Spectrometry*, vol. 38, pp. 510–512, Nov 2009.

[37] C. T. Chantler, M. N. Kinnane, C. Su, and J. A. Kimpton, "Characterization of K spectral profiles for vanadium , component redetermination for scandium , titanium , chromium , and manganese , and development of satellite structure for Z = 21 to Z = 25," *Physical Review A*, vol. 73, no. 012508, pp. 1–16, 2006.

[38] C. T. Chantler, M. N. Kinnane, J. D. Gillaspy, L. T. Hudson, A. T. Payne, L. F. Smale, A. Henins, J. M. Pomeroy, J. N. Tan, J. A. Kimpton, E. Takacs, and K. Makonyi, "Testing three-body quantum electrodynamics with trapped Ti^{20+} ions: Evidence for a Z-dependent divergence between experiment and calculation," *Physical Review Letters*, vol. 109, no. 15, pp. 1–5, 2012.

[39] G. Hölzer, M. Fritsch, M. Deutsch, J. Härtwig, and E. Förster, "K 1,2 and K 1,3 x-ray emission lines of the 3d transition metals," *Physical Review A*, vol. 56, no. 6, pp. 4554–4568, 1997.

[40] J. Kawai, T. Konishi, A. Shimohara, and Y. Gohshi, "High resolution titanium kα x-ray fluorescence spectra," *Spectrochimica Acta Part B: Atomic Spectroscopy*, vol. 49, no. 7, pp. 725 – 738, 1994.

[41] D. F. Anagnostopoulos, D. Gotta, P. Indelicato, and L. M. Simons, "Low-energy x-ray standards from hydrogenlike pionic atoms," *Physical Review Letters*, vol. 91, no. 24, pp. 12–15, 2003.

[42] C. T. Chantler, "X-ray diffraction of bent crystals in Bragg geometry. I. Perfect-crystal modelling," *Journal of Applied Crystallography*, vol. 25, no. pt 6, pp. 674–693, 1992.

[43] C. T. Chantler, "X-ray diffraction of bent crystals in Bragg geometry. II. Non-ideally imperfect crystals, modelling and results," *Journal of Applied Crystallography*, vol. 25, no. pt 6, pp. 694–713, 1992.

[44] C. T. Chantler and R. D. Deslattes, "Systematic corrections in Bragg x-ray diffraction of flat and curved crystals," *Review of Scientific Instruments*, vol. 66, no. 11, pp. 5123–5127, 1995.
[45] A. J. Illig, C. T. Chantler, and A. T. Payne, "Voigt profile characterization of copper Kα," *Journal of Physics B: Atomic, Molecular and Optical Physics*, vol. 46, no. 23, p. 235001, 2013.
[46] M. Deutsch, G. Holzer, J. Hartwig, J. Wolf, M. Fritsch, and E. Forster, "Ka and Kb x-ray emission spectra of copper," *Physical Review A*, vol. 51, no. 1, p. 283, 1995.
[47] M. H. Mendenhall, A. Henins, L. T. Hudson, C. I. Szabo, D. Windover, and J. P. Cline, "High-precision measurement of the x-ray Cu K α spectrum," *Journal of Physics B: Atomic, Molecular and Optical Physics*, vol. 50, no. 115004, pp. 1–18, 2017.

Appendix A. Electronics and Processing

The UM Backgammon detector relies on a sophisticated data acquisition system specifically developed for the detector and its use as part of our Johann-type curved crystal X-ray spectrometer. The design allows single photon counting over a wide range of count rates [30].

The data acquisition system used in the UM Backgammon detector takes the four outputs of the detector, two from the cathode and two from the anode. The four signals are integrated over four independent charge sensitive pre-amplifiers and balanced by independent shaping amplifiers. A universal coincidence module is used to determine signals from the same photon-gas event by matching pulses recorded within 0.2 μs. Two gate and delay generators are used, the first to enable the passing of the sampled and held, shaped and stretched data, the second enabling the acquisition. A PXI chassis with a 3MHz four-channel simultaneous-sampling 145 bit digitizer is used to digitise each analogue signal. The chassis is connected to a PC running labVIEW. The PC controls the hardware, calculates and outputs the encoded detector data, and stores raw data. A schematic of the system is shown in Fig. A1.

When the UM Backgammon detector is used with the Johann-type curved crystal spectrometer the data acquisition system also provides digitisation of the four inclinometers and temperature data. Importantly, this is done via a high-speed serial MXI-4 interface capable of sustained data transfer at a rate of 78 MB/s, allowing improved acquisition efficiency count rates in the 1 Hz-50 kHz range.

Appendix B. Signal Processing and Linearisation

For both experiments the data collection was performed using the electronic outputs of the University of Melbourne's Backgammon detector. For each photon-gas interaction, a region of the argon gas is ionised, an electron avalanche is created and recorded by the cathode board. The ionised gas particles are similarly measured by the anode wire. This produces a voltage reading at each end of the cathode board and anode wire giving four output voltages: Two voltages, A and B, from the anode wire and two, C and D, from the cathode board. The signal amplitudes are digitised and converted into a

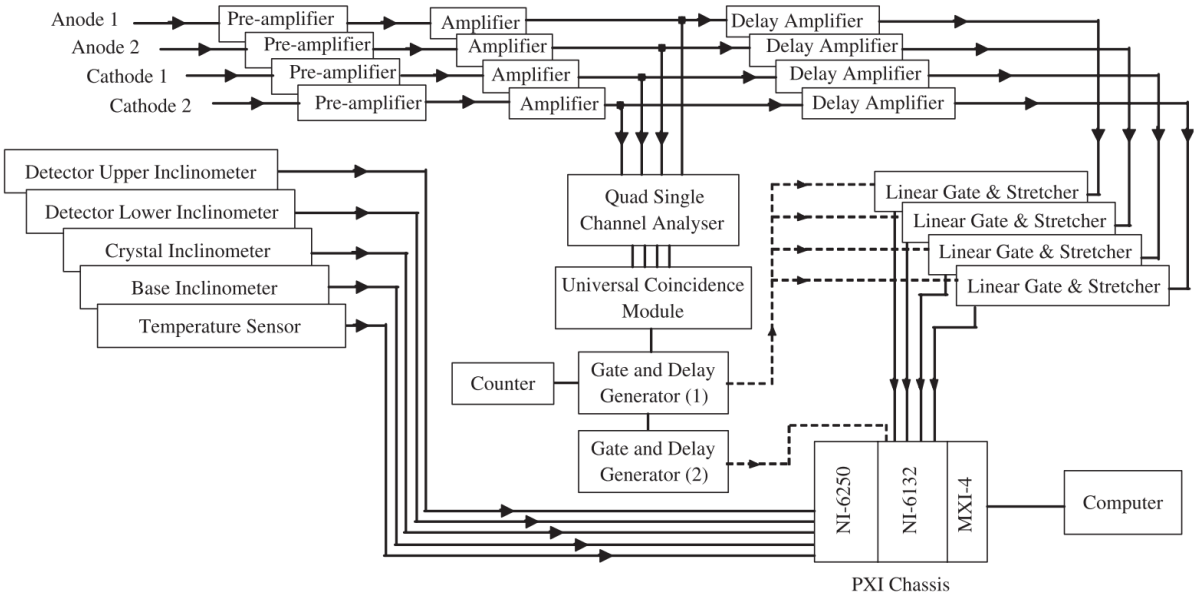

Figure A1. Schematic of the data acquisition system: detector signal processing electronics, inclinometers, temperature sensor and PXI chassis [30].

spatial position, x-y, on the detector through the equations:

$$x = \frac{C}{C+D};\ y = \frac{A}{A+B} \tag{B.1}$$

The detector face was partitioned in each direction into 1000 channels. Raw data could then be represented as a 2D histogram representing the number of photon-gas interactions occurring in each area of the detector. Fig. B1 illustrates the raw output for Cr Kα spectrum. The 13 distinct horizontal 'rows' are representative of the 13 anode wire segments of the detector; the two separate 'dots' within each wire are representative of distinct Kα_1 and Kα_2 lines. There are also additional counts along each of the anode wires due to noise and background.

The raw signal is structured at the top and bottom of the detector face. Sources of this spatial non-linearity include charge attenuation, asymmetric electric fields and bimodal charge distribution. While the backgammon detector has been designed to minimise these effects, the geometry of the device means that they are still present in the top and bottom wires due to non-uniform electric fields and edge effects prior to calibration, as with all similar detector types [20]. To correct this, the data must be linearised or the end wire segments deleted or left as guard rails.

The data from the backgammon detector was linearised using a calibration map. The map was created through a calibration experiment using the rotating anode at The University of Melbourne. Linearisation is needed to transform the x value, obtained from equation B.1, to the *input* position - where the photon hits the detector face. This is the purpose of the calibration map. The rotating anode was used to produce a Cu Kβ profile that was then collimated, passed through the monochromator and projected

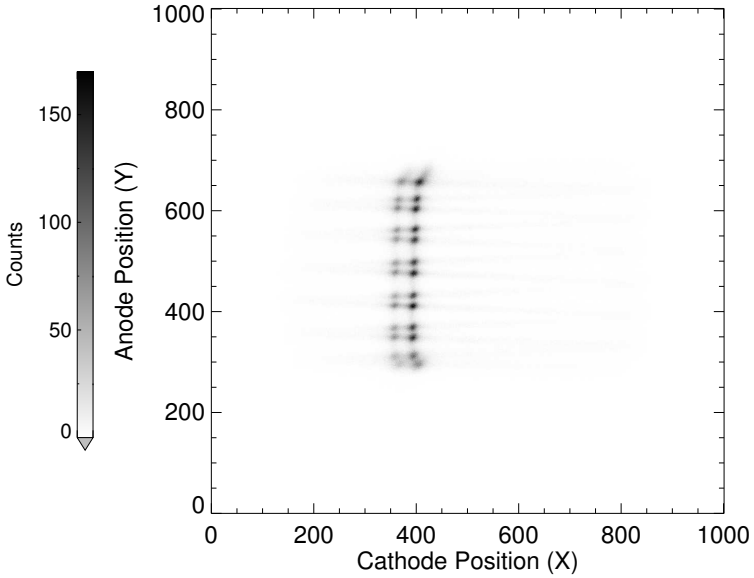

Figure B1. The raw, uncalibrated 2D histogram of Cr Kα, showing the photon-gas signal in the counters. These raw signals need calibration, like any detector, and illustrate wire components and near-edge field distortion. Edge or guard wire segments can be removed from analysis or corrected for as with all MWPC processing.

onto the detector face as in the Cu Kα experiment. The detector was mounted on a linear stage, such that when the linear stage shifted in the horizontal, the line source moved across the detector face illuminating a different vertical slice of the detector. The centre of the detector was found and the corresponding position of the linear stage (L) was defined as 0 mm. Profiles were taken from $L = -20mm$ to $L = 20mm$. A 2D histogram was created for each physical position L with the x-axis split into 1000 channels and the y-axis split into 500 rows. For each row a 1D histogram was created, showing the x position that the detector measured an X-ray event hitting the detector at L. A Gaussian was fitted to the histogram for each row. The position of this Gaussian could then be used as a measure of the output position x as a response to a photon hitting the detector at a physical position L. This relationship was in general different for each row. The difference between the output x value and the associated L is a measure of the non-linearity in the x direction in that row of the detector. To remove this non-linearity, a map was created to take x to L through a fitted polynomial for each row. Polynomials of degree 2 to degree 20 were investigated. Degree 11 was found to be sufficient and stable. These 500 polynomials (1 for each row) defined the calibration of detector response to an X-ray event happening at L. The result of the map is shown in Fig. B2.

The images were rotated, column summed and their full width at half maximum (FWHM) recorded. The rotation that gave the smallest FWHM was chosen for each

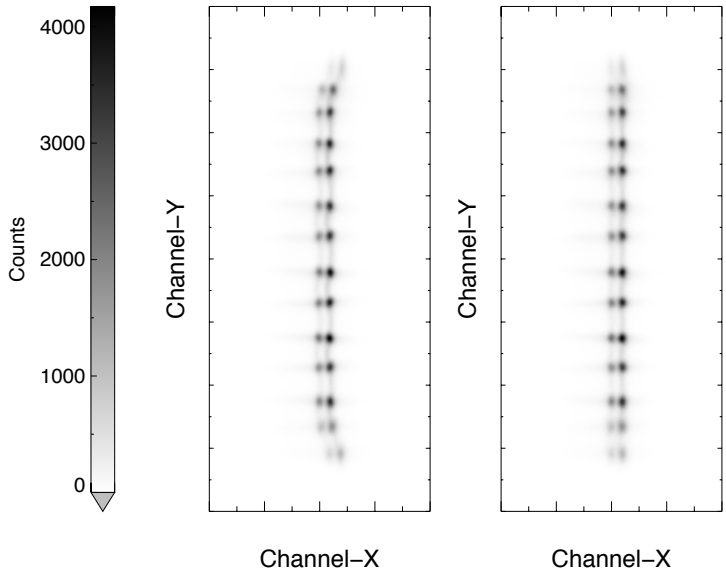

Figure B2. The left hand window shows the pre-processed image for the Cu data. The right hand window shows the corresponding linearized data. The 'dots' show the position of the Kα_1 (right) and Kα_2 (left) peaks on the backgammon's anode wires. Comparing the two images shows that distortions of the field and position are, unsurprisingly, dominated by the end wires at the top and bottom of the detector.

spectrum. For the Ti and Cr data this was found to be $-1.8°$. The Cu data were aligned well and required no rotation. Fig. B2 shows the end-wire distortion in the horizontal direction corrected by the linearisation map of the Cu data. The end anode-wires for the Ti and Cr data were removed before column summing. Similarly the Cr and Ti images required a horizontal shifting of the odd wires. The amount of shifting was determined by minimising the FWHM of Kα_1.

Appendix C. Linearity Tests and Details

Spatial linearity is an important feature of any detector as it enables accurate energy determination. In X-ray spectroscopy this allows the resolution of distinct energy peaks attributed to electronic transitions. Previous backgammon detector designs have quantified linearity in a number of ways. Payne *et al.* and Kimpton *et al.* both provide a thorough analysis of a linearity experiment similar to our own [31, 29].

The non-linearity of our detector after calibration can be quantified by plotting the centre of mass of the 1D histograms, taken in the calibration experiment, against the position on the detector that the image was taken, L. To measure the centre of mass of the 1D histogram each histogram was fitted with the sum of two Lorentzian functions plus a background constant. The centre of mass was then calculated on the

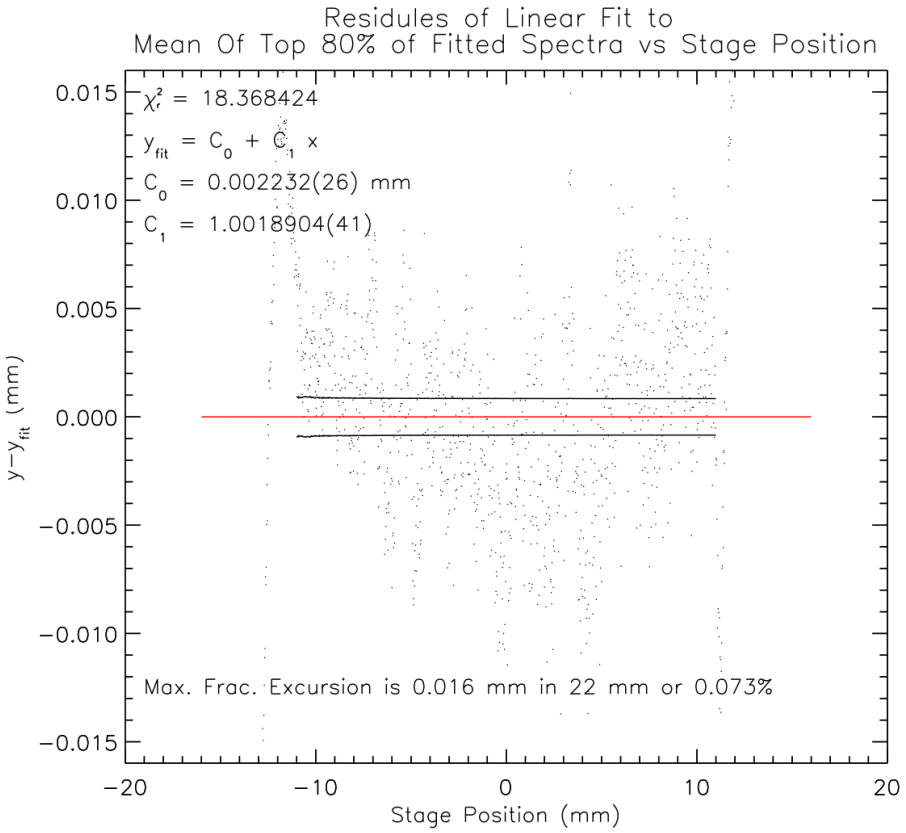

Figure C1. The residuals of a straight line fit of central tendency of the fitted spectra to the linear stage position are shown. The black lines are the uncertainty envelope of the central tendency.

fitted function above 20% of the maximum height.

A straight line was fitted to the centre of mass versus linear stage position (Eqn C.1). A line of best fit is used to model the relationship between the position on the detector that a Cu Kβ spectrum is taken and the position that the detector measures the event. The fit is defined to a small fraction of 0.01 μm showing a good stability over the active area.

Non-linearity can also be quantified by looking at the uncertainty in the parameters of the fit, the gradient and the offset. Payne *et al.* provide a fractional uncertainty in the fitted gradient of 0.019% and 0.005% in the offset, while Kimpton *et al.* report a fractional uncertainty for both fitted parameters of 0.0001%. The fractional uncertainty in our fitted parameters are: 1.165% for the offset and 0.00041% for the gradient.

$$y_{fit} = (1.0018904 \pm 0.0000041) \times StagePosition + (0.002232 \pm 0.000026) mm \quad \text{(C.1)}$$

The residuals give a measure of the non-linearity of measurement after calibration. The *maximum fractional non-linearity* is defined as the maximum residual between the detector output, x, and physical length, L, at which the event took place, divided by the total length of the active region of the detector. [30] demonstrate a maximum fractional non-linearity of 0.2%. Similarly [32] provide a value of 0.345%. Our maximum is a

significant improvement on both of these. The maximum residual in the 22 mm active region of our detector was 16 μm, giving a fractional non-linearity value of 0.073%. All residuals within the effective active region of the detector (the middle 22 mm) were below 16 microns and almost all within 10 microns (Fig. C1). This gives a quantitative value for the non-linearity, over the active region, of at most, the *maximum fractional non-linearity*, of 0.073%. For the relevant Cu Kβ spectrum, used in the linearity test, 0.073% corresponds to fifty parts per million in energy. Good statistics and the use of a larger bin size means that even the worst case scenario is much more accurate than 50 ppm.

[32] defines the *regional differential non-linearity* as the mean of the experimental residual from the model after box-car filtering over 11 points. This measure is useful as it suppresses random statistical noise leaving a measure of the typical excursion from the detector output and the fit.

[32] define the *regional non-linearity* as the average deviation of the detected centroid from the linear fit and provide this as a percentage to be 0.068%. This measure represents the typical error of a single channel position determination. [30] estimate a regional non-linearity of 0.025%. In Fig. C1 we see this to be approximately 1 μm or 0.0045%. This is a robust estimate of the error of a broad feature in a map, and represents an uncertainty for the measurement of Cu Kα of about 2 parts per million in energy.

Appendix D. Background subtraction

The raw Cu data, taken with the rotating anode source, contained two components. The Cu Kα spectrum and also higher energy background or scattered X-rays. To isolate these a high attenuation background exposure was taken. This background could then be modelled in the fitting process along with the other components of the spectra, Kα_{ij}, adding one parameter to the fitting function, a scale to control the magnitude of the background present in the data. The background component was largely proportional to exposure (time $\times$ current) and was attenuated partly by the foils, consistent with being a higher energy component.

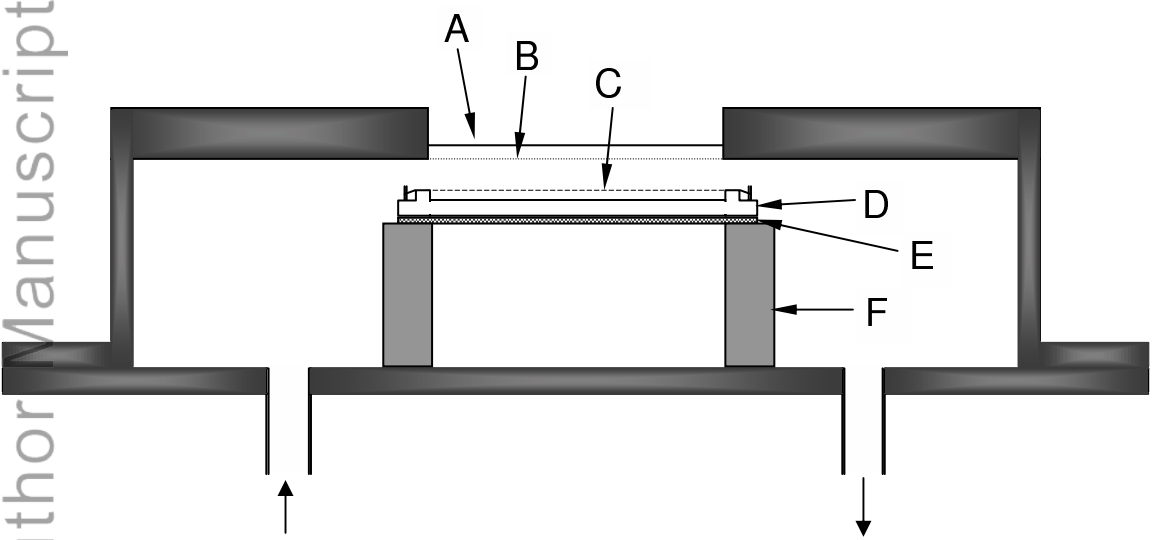

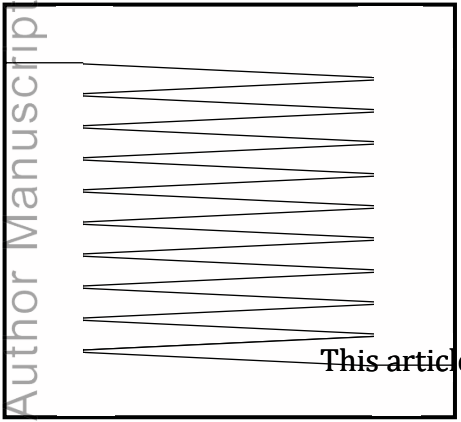

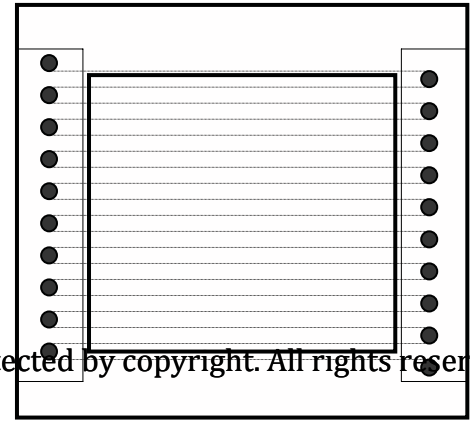

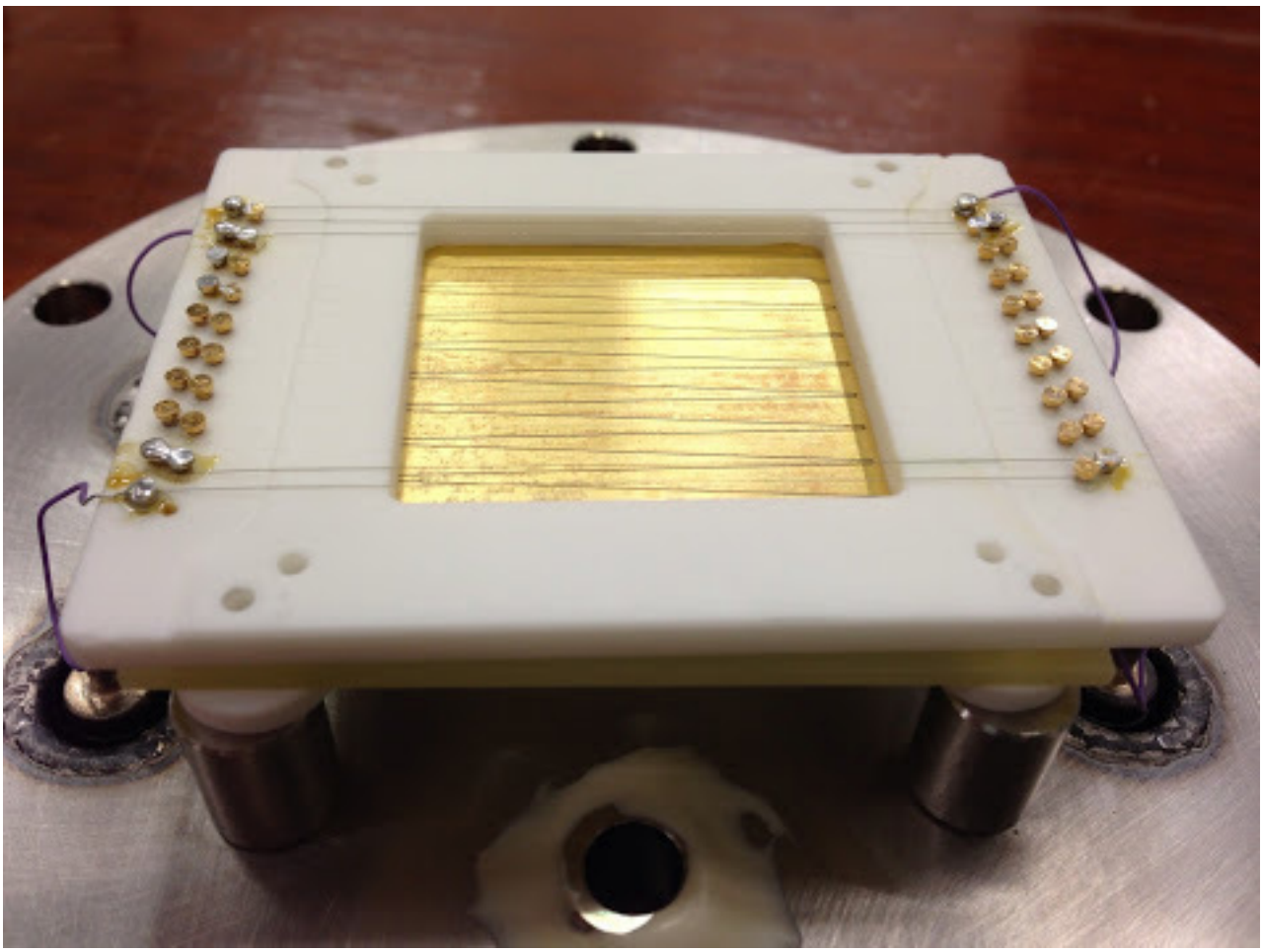

xrs-18-0095-File004.JPG

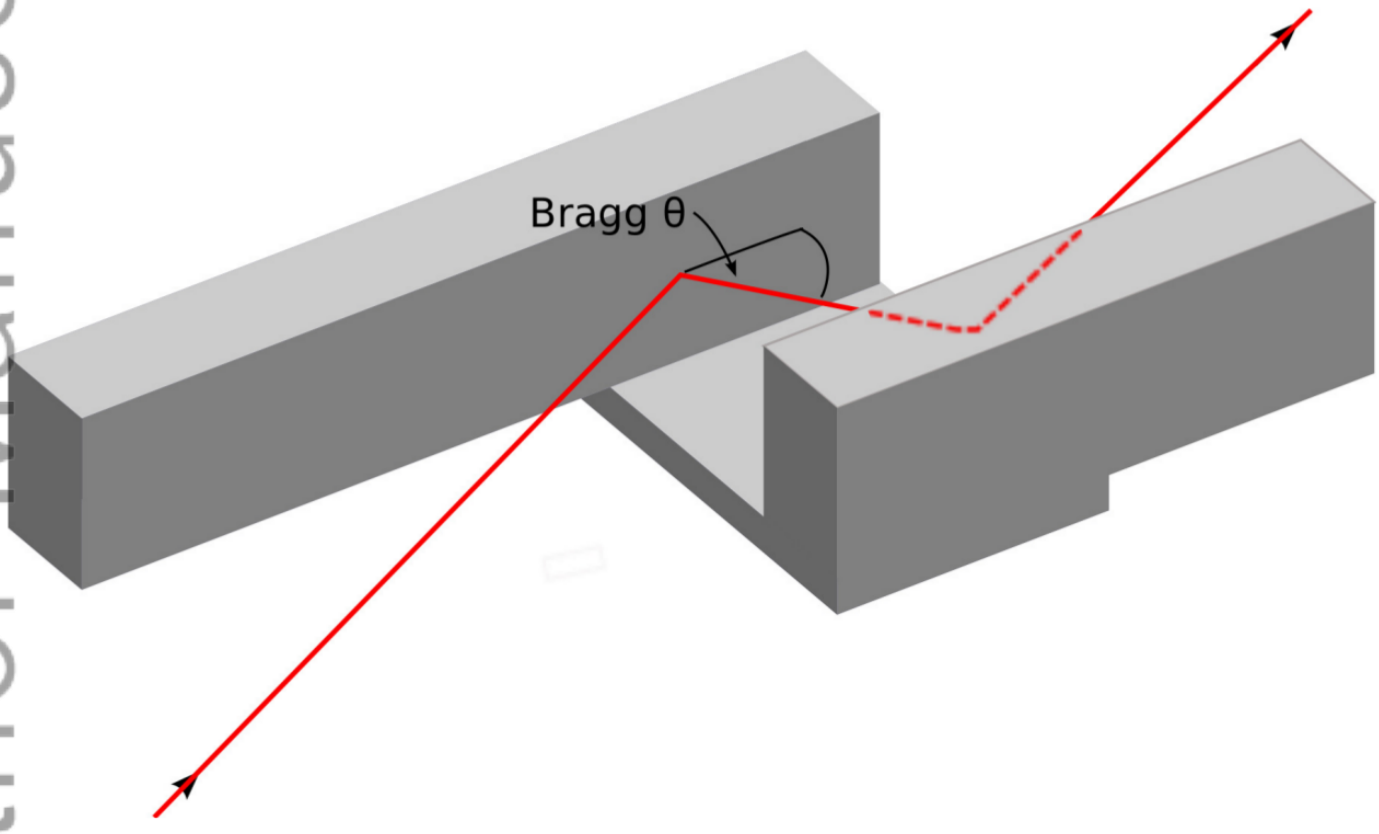

xrs-18-0095-File005.png

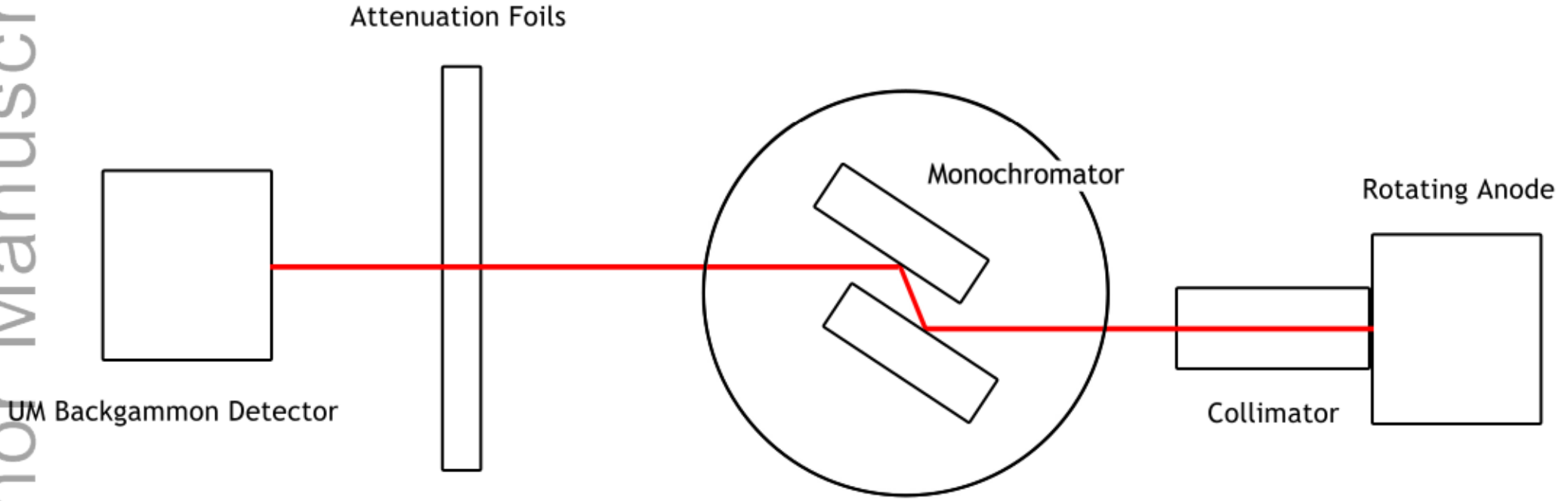

Fit of Attenuation Curve

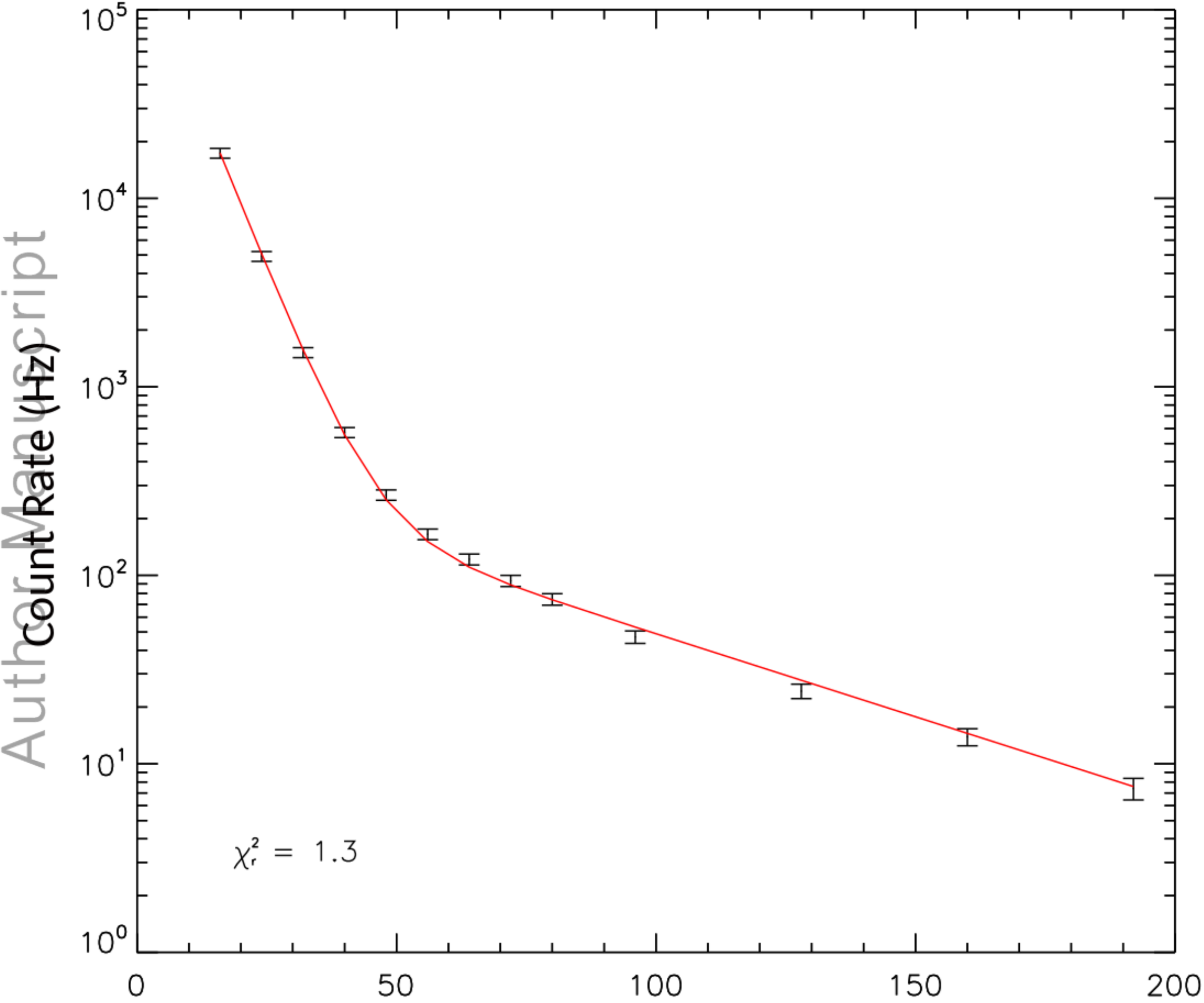

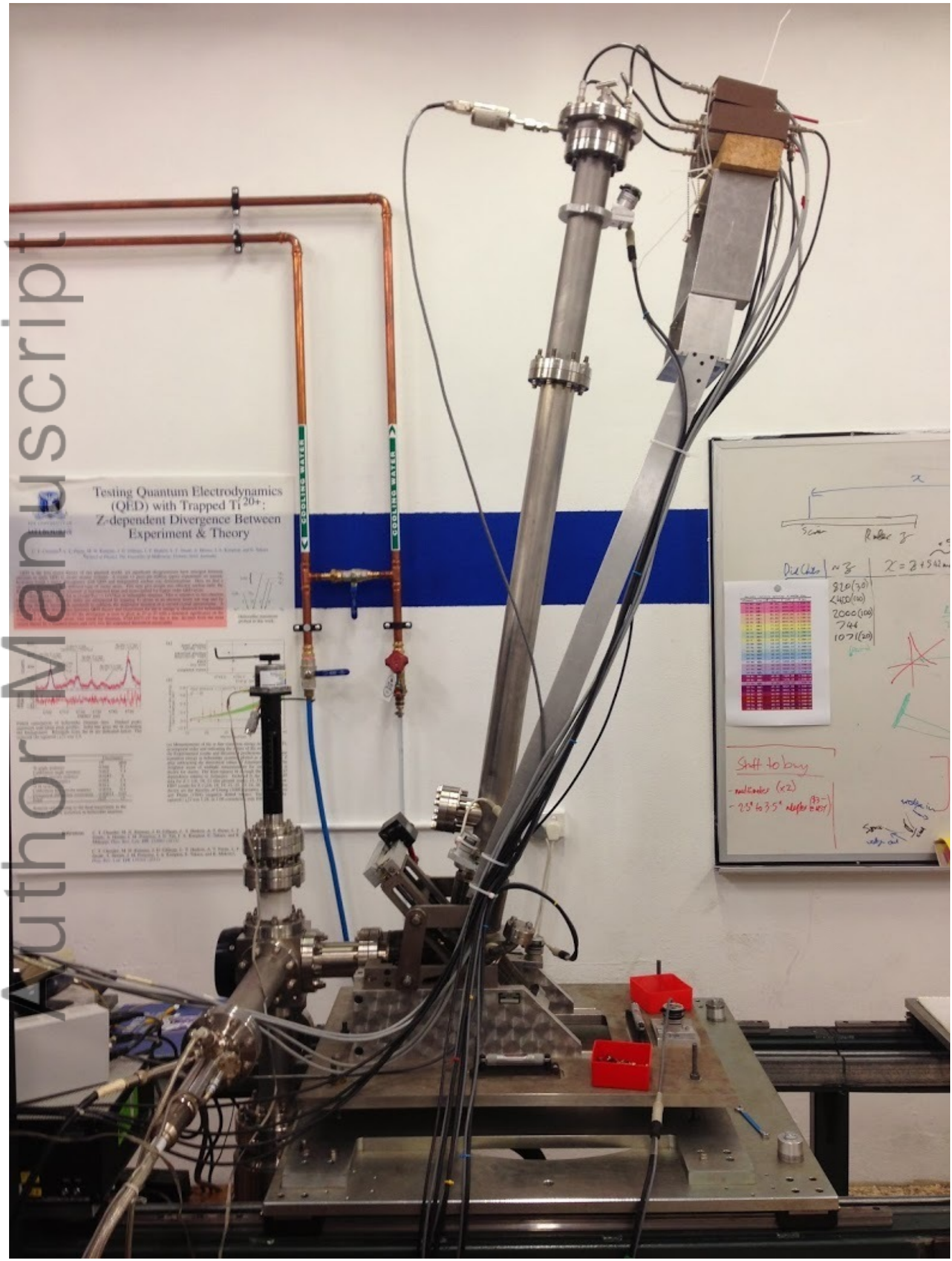

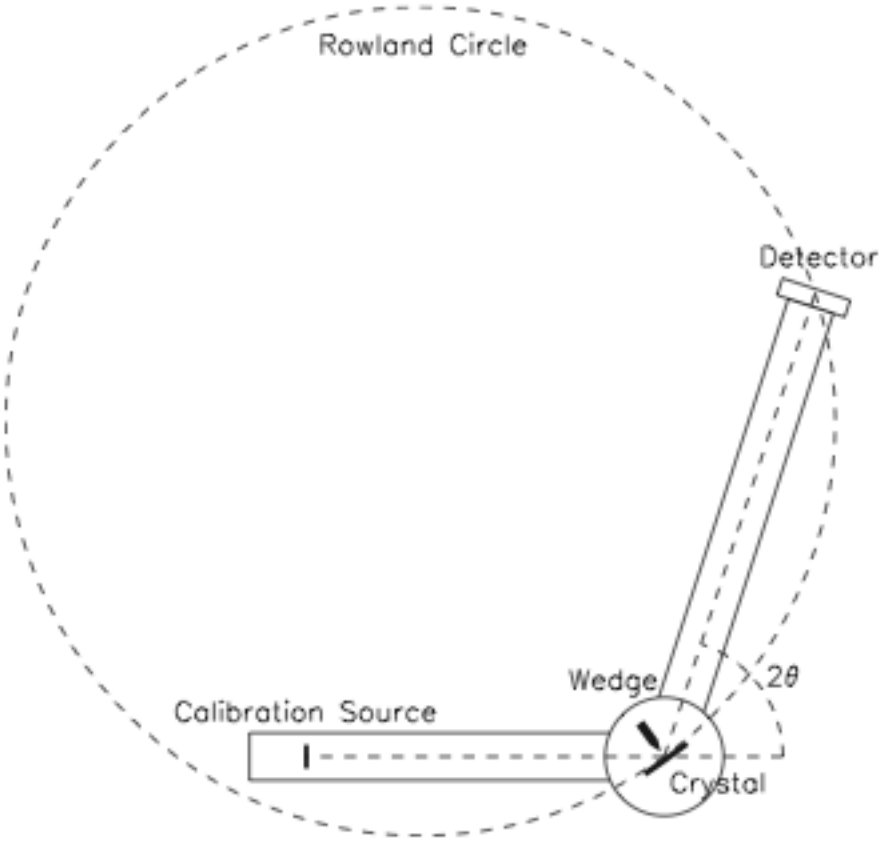

xrs-18-0095-File009.png

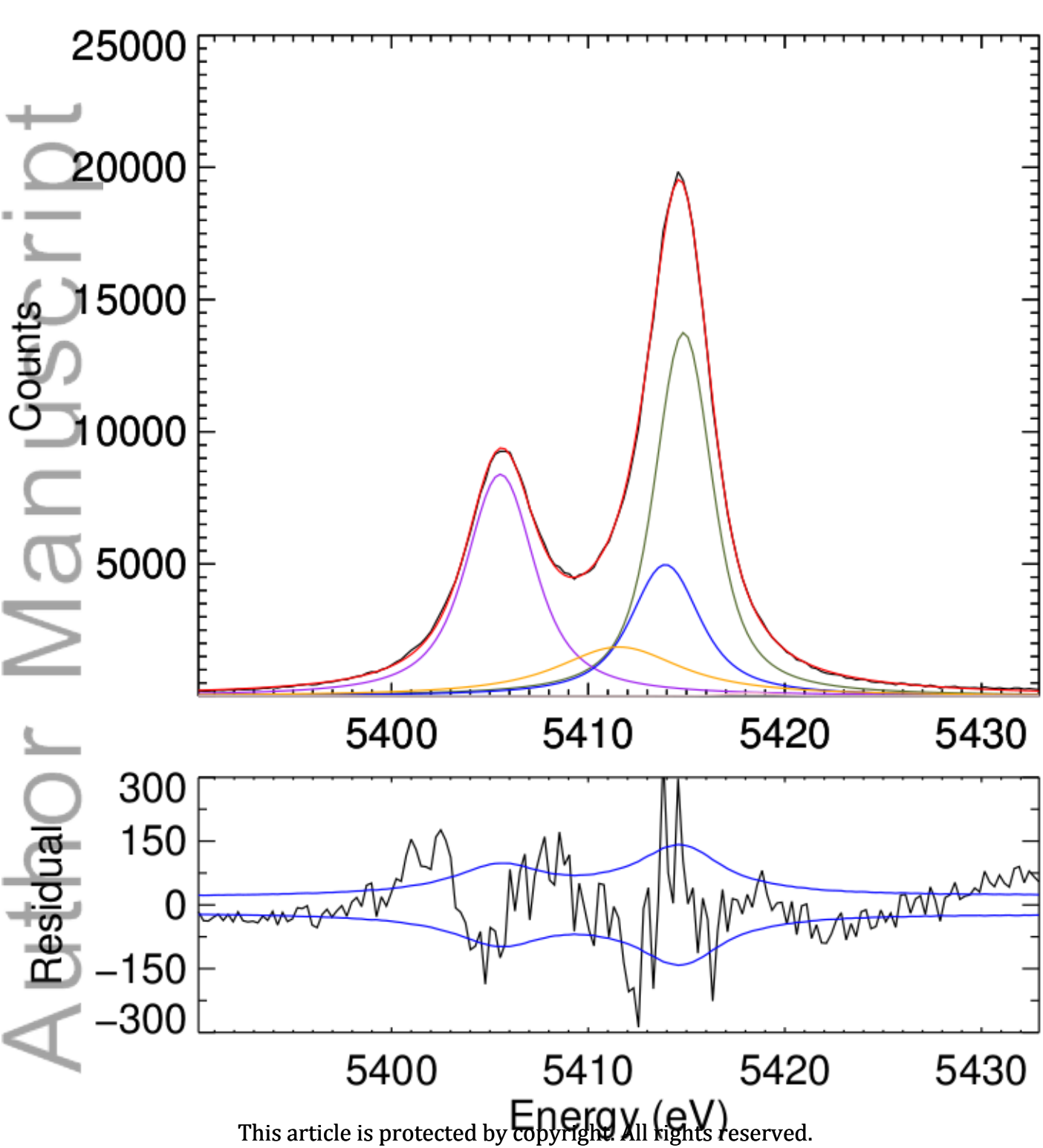

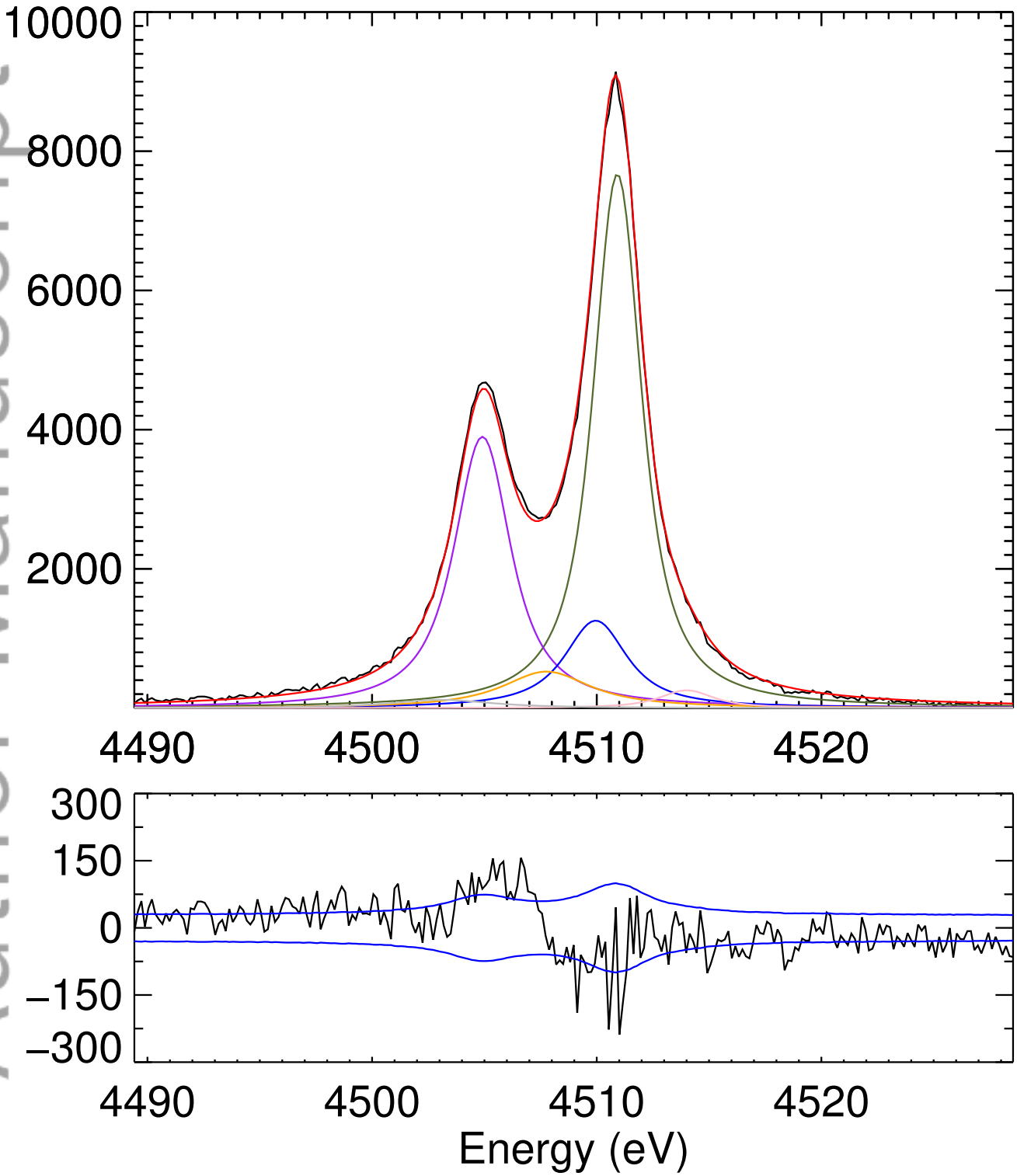

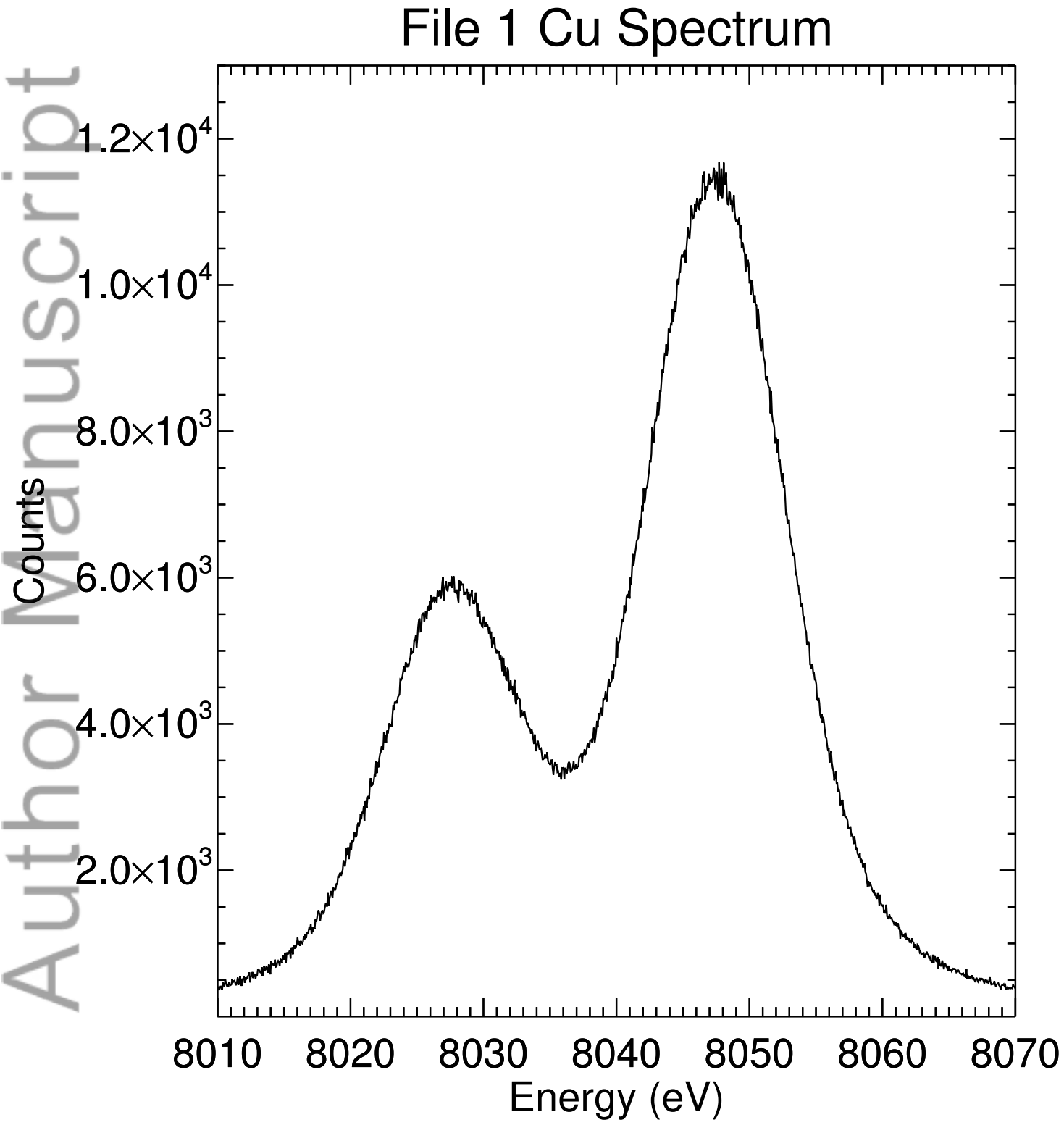

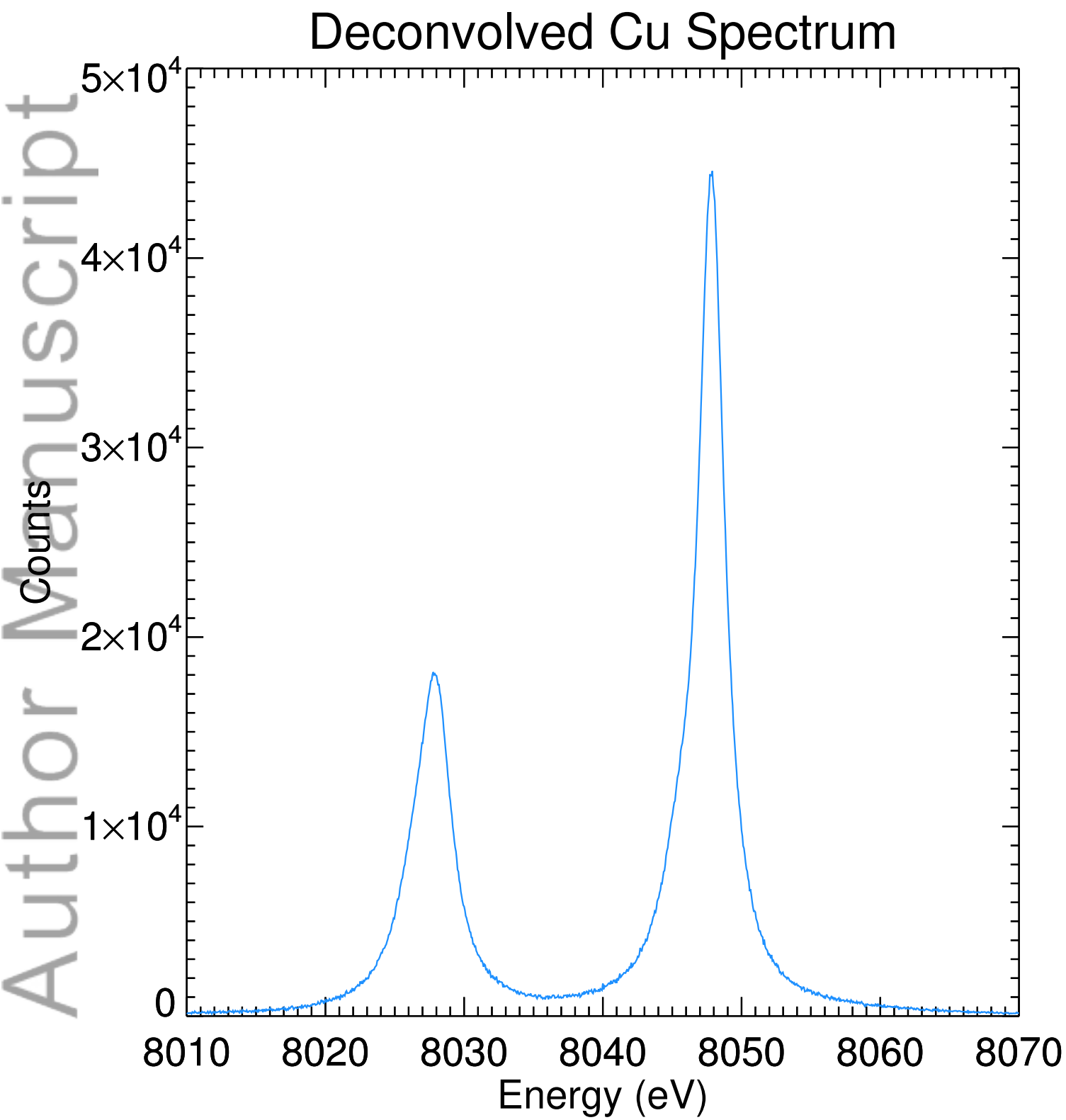

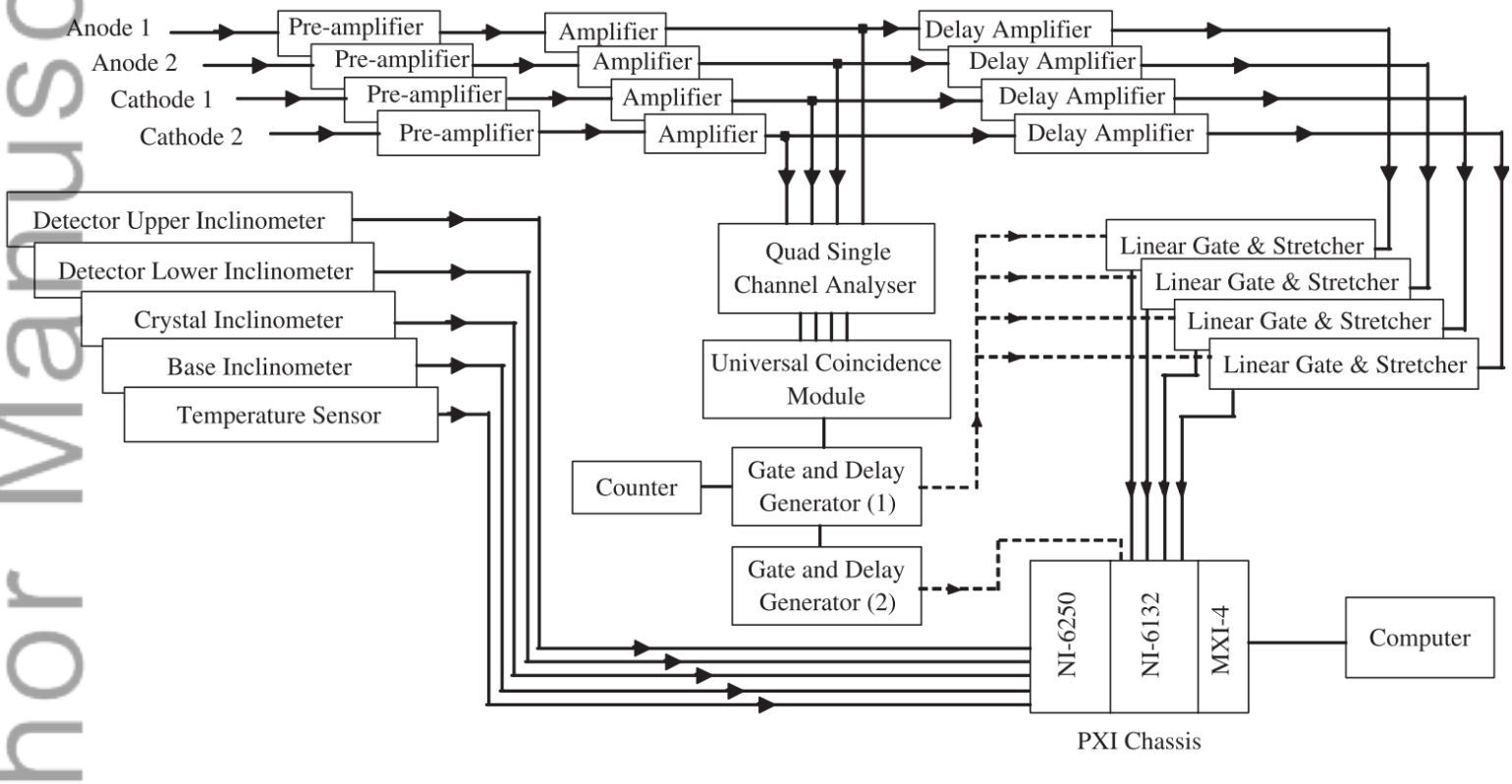

xrs-18-0095-File014.png

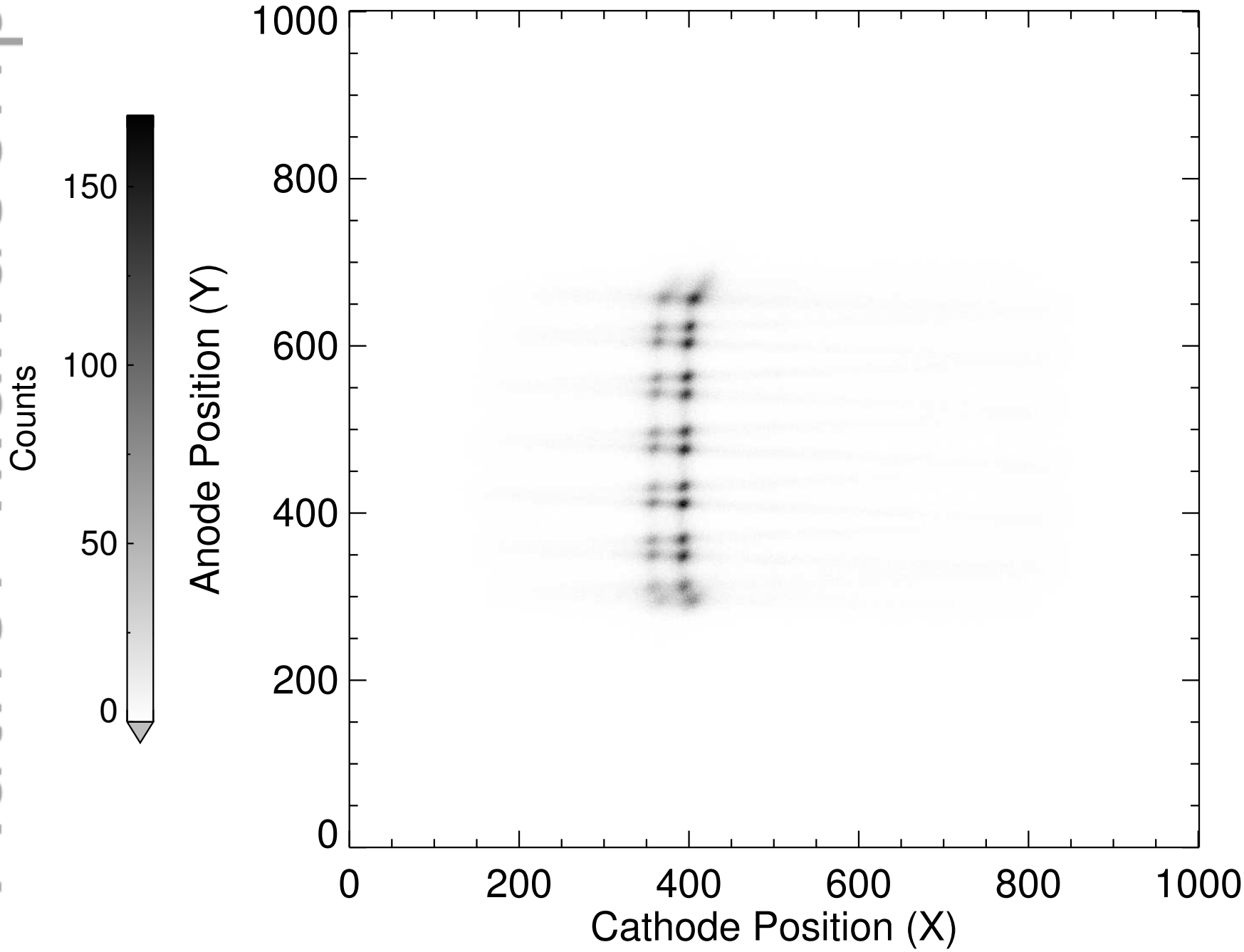

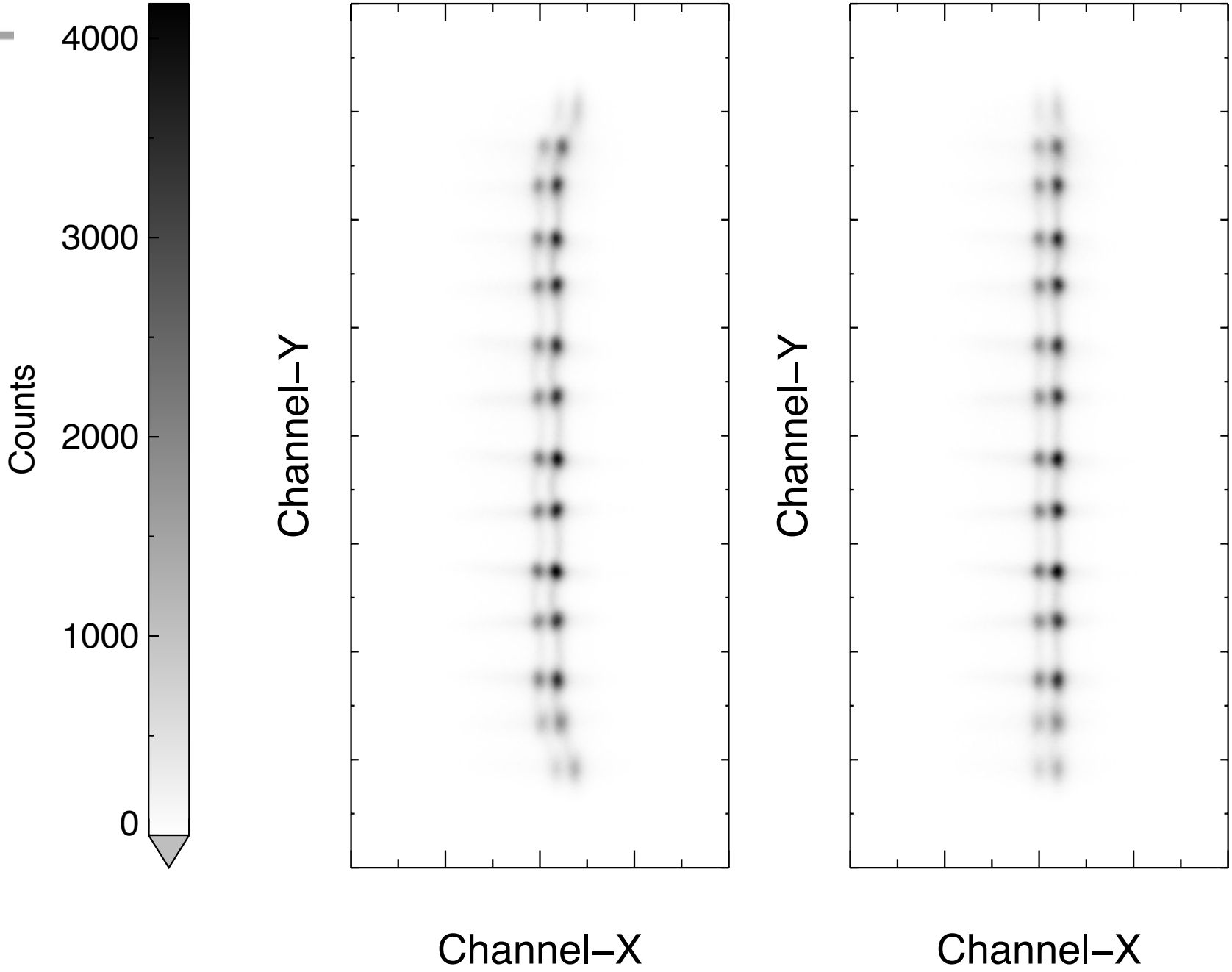

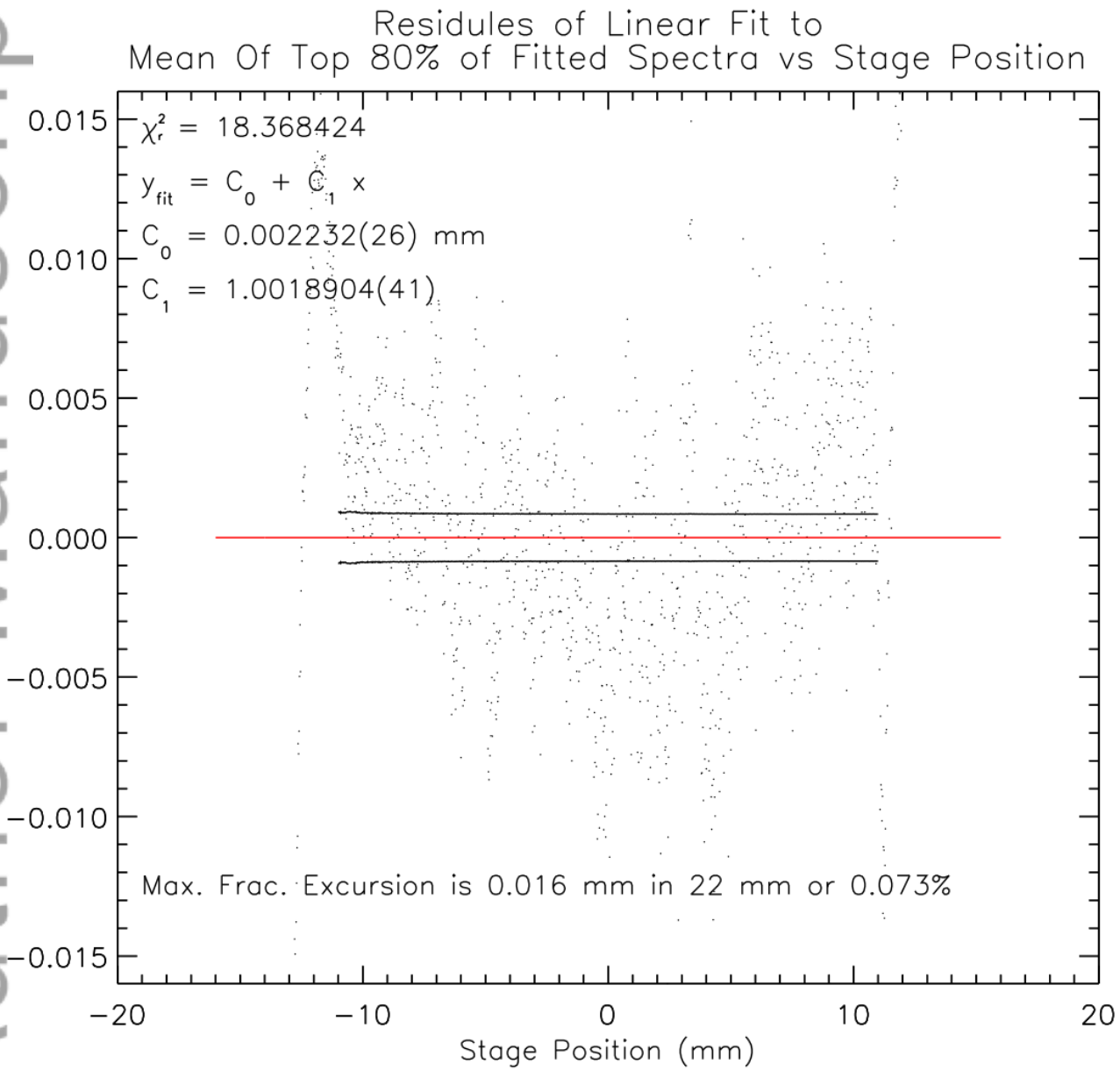

xrs-18-0095-File017.png